Tools for numerical modelling of nonlinear propagation in hollow capillary fibres and their application

IOP Publishing Journal of Optics
J. Opt. **25** (2023) 024005 (19pp) https://doi.org/10.1088/2040-8986/acab13

Tools for numerical modelling of nonlinear propagation in hollow capillary fibres and their application

Aurora Crego[1,2,*], Julio San Roman[1] and Enrique Conejero Jarque[1]

[1] Grupo de Investigación en Aplicaciones del Láser y Fotónica, Departamento de Física Aplicada, Universidad de Salamanca, E-37008 Salamanca, Spain
[2] Institute for Photonics and Nanotechnologies, IFN-CNR, Milano 20133, Italy

E-mail: acrego@usal.es

Received 12 August 2022, revised 23 November 2022
Accepted for publication 13 December 2022
Published 3 January 2023

Abstract

The development of new coherent and ultrashort light sources is of great relevance for exploring fundamental processes and different applications in science. The most successful technique for generating ultrashort laser pulses, in terms of energy and pulse duration, is using hollow capillary fibre (HCF) compressors. The different strategies to further increase the pulse energy and to achieve shorter pulses at non-conventional wavelengths, lead to continuous improvement of this technique. In this work, we present the theoretical framework of the nonlinear propagation in HCFs through the propagation equation and the spatio-temporal effects that appear in the nonlinear dynamics. To numerically study the nonlinear propagation of the pulse in the HCF, we present different numerical models considering only the spatial effects, (1 + 1)D model, the full spatio-temporal dynamics and ionization, (2 + 1)D model, or the case with lack of cylindrical symmetry, (3 + 1)D model. To show the performance of some of these models in a particular case, we study the generation of ultrashort and energetic dispersive waves (DWs) inside the HCF. We show that the emission of a DW at a fixed wavelength for different pump wavelengths is possible by parameter scaling.

Keywords: nonlinear optics, hollow capillary fibres, numerical simulations, GNLSE, dispersive wave emission

(Some figures may appear in colour only in the online journal)

1. Introduction

Over the last 60 years, the possibility of generating new ultrafast and ultrabroadband light sources to explore different phenomena in science has been one of the main goals in the scientific community. In particular, ultrashort laser pulses are useful for a great number of applications due to their very short duration, so they can be used to induce and measure ultrafast phenomena with femtosecond time resolution. In this work, we will focus on the basics of the techniques to generate these ultrashort pulses.

The invention and continuous development of laser systems motivated the search for new applications. One of the most important was the use of optical fibres for pulse post-compression, as the pulse propagates over long interaction lengths enhancing the nonlinear response [1]. Using these optical fibres, a breakthrough for ultrafast science was reported with the first post-compression of a laser pulse down to 6 fs after spectral broadening due to the self-phase modulation effect [2, 3]. However, the possibility of generating short pulses with energies above the nanojoule level with these

* Author to whom any correspondence should be addressed.

devices was challenging. This limitation, together with the possibility of generating more intense and shorter laser pulses using the Chirped Pulse Amplification technique [4], led to the research of new fibre designs.

Significant progress in energy scaling was possible with the invention of photonic crystal fibres (PCFs) [5]. These devices provide exceptional control of pulse dispersion and, in addition, they have an extremely small core (with a cross-section of a few μm^2) that enhances the nonlinearity and can be hollow, providing a higher damage threshold compared to standard optical fibres [6]. Once that the few-femtosecond pulse regime was achieved with these PCFs, the interest in even more energetic few-cycle laser pulses for different applications motivated the research of new techniques to scale the pulse energy up to the millijoule level.

The most commonly used method to generate these ultrashort, energetic pulses is through gas-filled hollow capillary fibres (HCFs), which is the topic of this work. A simple scheme of a HCF compressor is shown in figure 1. This technique was proposed and experimentally demonstrated by Nisoli *et al* [7]. The energy of the generated few-cycle pulses was more than three orders of magnitude higher than that obtained in previous experiments. This was possible due to the low nonlinearity of the gas medium inside the HCF and the increment of the core size compared to PCFs. Although this technique is well known, the search for different strategies to scale the output pulse energy up and to obtain ultrashort pulses at non-conventional wavelengths leads to further investigation of this technique.

1.1. Pulse post-compression in HCFs

One of the advantages of the HCF is the interaction of laser pulses with a gas medium, since it has a higher damage threshold than other nonlinear media and is not permanently damaged if ionized. For these reasons, HCFs and hollow-core PCFs have been a successful tool in this post-compression context in the last decades. Another main advantage of both devices is that the nonlinearity and dispersion of the system can be easily tuned by simply changing the gas pressure or the type of gas inside the fibre. Compared to hollow-core PCFs, large-core HCFs (larger than 100 μm) are used when propagating intense (millijoule-scale) laser pulses over lengths of a few meters. However, HCFs present higher propagation losses, as the guiding is based on grazing-incidence reflection and it is very sensitive to bending. There is a limit on the input pulse energy to avoid detrimental nonlinear effects, such as self-focusing and plasma [8] that worsen the compression of the output pulse. Despite these limitations, the output pulses from HCFs are essential, for instance, to generate isolated attosecond pulses via high-order harmonic processes in noble gases [9].

In the last decades, several advances related to pulse duration and energy scaling in HCF compressors have been achieved with different strategies, such as using short input pulses [10], circular polarization [11] or two-stage HCF

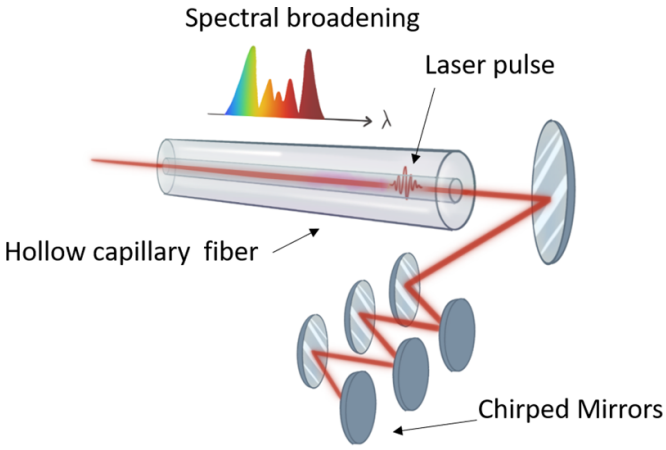

Figure 1. Post-compression scheme based in HCFs technique.

configurations [12, 13]. In terms of energy scaling, gas ionization sets an upper limit on the input peak intensity of the pulse to avoid detrimental nonlinear effects in the propagation, which at the same time restricts the HCF core size. However, for a chosen core size, to obtain the desired spectral broadening it is possible to change the type of gas, its pressure or the HCF length to enhance the nonlinearity. Increasing the gas pressure is also a constraint, since it is convenient to avoid the critical value at which self-focusing occurs. A possible solution to this problem is to use pressure gradients inside the HCF to avoid self-focusing and ionization of the gas at the HCF entrance. The strategy is to apply the gas at the output side and it flows to the entrance through the fibre, but with the disadvantage of reducing the effective interaction length [14]. On the other hand, it is possible to increase the HCF length, but the bending of the fibre itself sets a limit. This problem was solved by using flexible HCFs, whose ends can be pulled to keep the fibre straight [15]. By combining all the methods mentioned above for energy scaling, it is possible to obtain compressed pulses of 3.8 fs and 6.1 mJ with a peak power of 1.2 TW [16].

A different method to obtain high-energy pulse compression, while avoiding the ionization of the medium, is the propagation of long input pulses of a few hundred femtoseconds. Nevertheless, to compress them to the few-cycle regime, a large compression ratio is needed. It has been reported that the use of molecular gases, and taking advantage of the non-instantaneous nonlinear Raman response related to the alignment of molecules in the field direction, enhances the red side of the spectrum. This technique can be improved to obtain a two-octave spectrum and a compression factor of 45 [17].

In general, HCF postcompression is one of the most successful techniques, being able to reach the high-energy few-cycle regime with above-mJ and sub-3-cycle pulses [16, 18].

1.2. Pulse soliton self-compression in HCFs

An alternative nonlinear compression technique would be the soliton self-compression dynamics during nonlinear

propagation inside the HCF. With this technique, it is possible to obtain few-cycle pulses with multi-octave spectral spanning without the need for additional phase compensation after the HCF. However, the self-compression dynamics is highly dependent on the parameters of the input pulse and HCF, since the laser pulse must propagate in the anomalous dispersion regime inside the HCF. During the pulse propagation, the anomalous dispersion experienced by the pulse can be balanced by the self-phase modulation effect, leading to the soliton formation and soliton self-compression process that results in an ultrashort pulse with a high intensity peak. The maximum possible compression is limited by higher-order linear and nonlinear effects that can cause the break-up of the soliton into its fundamental components, a phenomenon known as soliton fission [19].

This technique has been studied in detail for infrared pulses in filaments [20], bulk material [21] and PCFs [22]. In HCFs, this process has been reported by Travers' group obtaining much higher soliton self-compression energy after carefully choosing the HCF and laser parameters [23]. To select the right parameters for the self-compression effect, we have to take into account that the linear dispersion experimented by the laser pulse inside the HCF depends on the gas dispersion and the HCF contributions. Moreover, the nonlinear response depends not only on the gas properties and pressure configuration [24], but also on the mode confinement. For instance, since both linear and nonlinear propagation properties depend on the spatial profile of the beam inside the capillary (see section 2.3 for an explanation of the HCF spatial modes), the use of high order hybrid modes [25–27] or structured beams with different number of lobes [28, 29] have been proposed to obtain self-compression in HCFs.

Travers's group has scaled the soliton effects to the multi-millijoule energy level and terawatt peak power level, orders of magnitude above optical fibres and PCFs. They experimentally observed the self-compression of a 10 fs laser pulse, previously post-compressed, down to 1.2 fs in a 3 m flexible HCF with 125 μm inner radius filled with 0.4 bar of helium. In addition, they generated tunable few-cycle ultraviolet pulses by changing the gas pressure. This effect is observed at the point of maximum compression, when the soliton fission occurs. At the same time, part of the energy is transferred resonantly from the soliton to a certain frequency in the normal dispersion region, separated from the soliton spectrum, in a phase-matching process. This effect, named dispersive wave (DW) generation, sets the foundations for a new topic in nonlinear optics due to the possibility of generating ultrashort tunable pulses in the ultraviolet. Wavelength-tunable DW emission from the ultraviolet to the infrared has also been demonstrated in gas-filled PCFs [30, 31], antiresonant PCFs [32] and also in downscaled HCF systems [33].

Usually, the way of generating these UV pulses for different applications is through frequency-conversion schemes, such as those using nonlinear crystals [34, 35], high-harmonic generation [36], selecting the desired wavelength from a broadband spectrum [37] or through the four-wave mixing [38] and third-harmonic generation in gases [39]. In general, these techniques are limited by the optical damage to the material and the post-compression setups, making the generation of ultrashort and energetic pulses in this spectral region with these techniques challenging. DW generation in HCFs has several advantages compared to the previous ones: the wavelength can be tuned through the fibre geometry, gas species and pressure, the conversion efficiency is higher than in the high-harmonic process and its duration can be only a few femtoseconds at the generation [40]. In addition, HCFs have broad ultraviolet transparency and a high damage threshold, which allows scaling up the energy. The tunability of the DW makes this emission an important tool for different applications, such as photoelectron spectroscopy and attosecond spectroscopy, as it is currently the only technique that allows to obtain UV pulses shorter than 5 fs at the microjoule level.

In this work we will present the theoretical basis and numerical methods to model the nonlinear propagation of short laser pulses inside HCFs. In section 2, we will present the pulse propagation equation and some of the HCF spatial modes. In section 3, we will explain in detail the $(1+1)$D, $(2+1)$D and $(3+1)$D numerical models for different scenarios. Finally, we will apply these models to simulate the DW emission at a fixed wavelength for different pump wavelengths in section 4.

2. Theoretical methods

In the present section we derive the equation that governs the pulse nonlinear propagation in HCFs. This equation describes the propagation of an ultrashort laser pulse through a nonlinear dispersive medium.

The propagation of an electric field in a dielectric, homogeneous and isotropic medium can be described by the wave equation derived from Maxwell's equations [41]:

$$\boldsymbol{\nabla^2 E} - \mu_0 \frac{\partial^2 \boldsymbol{D}}{\partial t^2} = 0 \tag{1}$$

where $\boldsymbol{E}$ is the electric field, μ_0 is the vacuum permeability and $\boldsymbol{D} = \epsilon_0 \boldsymbol{E} + \boldsymbol{P}$ is the displacement field (or electric flux density), being, ε_0 the vacuum permittivity and $\boldsymbol{P}$ the polarization vector. The displacement field, $\boldsymbol{D}$, represents the response of the bound charges in the medium to the effect of the propagating electric field, which induces an electric dipole moment. Considering the linear and nonlinear response of the polarization vector, $\boldsymbol{P} = \boldsymbol{P^L} + \boldsymbol{P^{NL}}$, we can express the displacement field as $\boldsymbol{D} = \boldsymbol{D^L} + \boldsymbol{P^{NL}}$, where $\boldsymbol{D^L} = \epsilon_0 \boldsymbol{E} + \boldsymbol{P^L}$ would be a linear displacement field. Introducing these expressions into equation (1)

$$\boldsymbol{\nabla^2 E} - \frac{1}{c^2}\frac{\partial^2 \boldsymbol{D^L}}{\partial t^2} = \frac{1}{\epsilon_0 c^2}\frac{\partial^2}{\partial t^2}\boldsymbol{P^{NL}} \tag{2}$$

where c is the speed of light in vacuum. From equation (2) we deduce that the polarization acts as a source of the electromagnetic field. If the intensity of the field applied to a dielectric material is high enough, the response of this material to

light becomes nonlinear. The origin of this nonlinear response is mainly related to the anharmonic motion of bound electrons under the interaction with the applied field. However, we can assume that $\boldsymbol{P}^{\boldsymbol{NL}}$ is treated as a small perturbation to $\boldsymbol{P}^{\boldsymbol{L}}$ since, for instance, the changes in the refractive index due to the nonlinear effects are $<10^{-6}$ [41]. To study the propagation of short laser pulses inside a HCF, both dispersive and nonlinear effects must be considered. The linear and nonlinear part of the polarization vector are related to the electric field by

$$\boldsymbol{P} = \boldsymbol{P}^{\boldsymbol{L}} + \boldsymbol{P}^{\boldsymbol{NL}} = \epsilon_0 \chi^{(1)} \cdot \boldsymbol{E} + \epsilon_0 \left(\chi^{(2)} : \boldsymbol{EE} + \chi^{(3)} \vdots \boldsymbol{EEE} + \ldots \right) \quad (3)$$

where $\chi^{(j)}(j = 1, 2, \ldots)$ is the jth order susceptibility, which in general is a tensor of rank $j+1$. We also assume that the electric field maintains the polarization along the propagation inside the HCF, so that a scalar approach is valid. Since the pulse is going to propagate through a cylindrical HCF filled with gas as nonlinear medium, the Laplace operator in equation (2) has the form $\nabla^2 = \partial^2/\partial z^2 + \partial^2/\partial r^2 + (1/r)\,\partial/\partial r + \left(1/r^2\right)\partial^2/\partial\theta^2$ in cylindrical coordinates. We can express both the electric field and the nonlinear polarization vector as:

$$\boldsymbol{E}(r,\theta,t,z) = \boldsymbol{A}(r,\theta,t,z) e^{i(k_0 z - \omega_0 t)} + c.c \quad (4)$$

$$\boldsymbol{P}^{\boldsymbol{NL}}(r,\theta,t,z) = \boldsymbol{p}^{\boldsymbol{NL}}(r,\theta,t,z) e^{i(k_0 z - \omega_0 t)} + c.c \quad (5)$$

where ω_0 is the central frequency of the pulse, $k_0 = n_0\omega_0/c$ is the wavevector and $n_0 = n_L(\omega_0)$ is the linear refractive index of the medium at ω_0. The expressions for $\boldsymbol{E}$ and $\boldsymbol{P}^{\boldsymbol{NL}}$ represent non-plane waves with complex time- and space-dependent varying amplitudes, $\boldsymbol{A}(r,\theta,t,z)$ and $\boldsymbol{p}^{\boldsymbol{NL}}(r,\theta,t,z)$.

We assume that $\boldsymbol{D}^{\boldsymbol{L}}$ and $\boldsymbol{E}$ in the frequency domain are related by the linear dispersion relation $\tilde{\boldsymbol{D}}^{\boldsymbol{L}}(r,\theta,\omega,z) = \epsilon_0 \epsilon^{(1)}(\omega)\tilde{\boldsymbol{E}}(r,\theta,\omega,z)$, where $\epsilon^{(1)}(\omega)$ is the linear relative permittivity, a dielectric complex scalar quantity in the case of a dissipative and isotropic medium. It is possible to define the complex refractive index of the medium as $n^2(\omega) = \epsilon^{(1)}(\omega)$, considering low losses inside the HCF in the wavelength region of interest, so the imaginary part of $\epsilon(\omega)$ is small compared to the real part. Doing the Fourier Transform of $\boldsymbol{D}^{\boldsymbol{L}}$, $\boldsymbol{E}$ and $\boldsymbol{P}^{\boldsymbol{NL}}$ and using the linear dispersion relation in equation (2), we can obtain the Helmholtz equation in the frequency domain

$$\nabla^2 \tilde{\boldsymbol{E}}(r,\theta,\omega,z) + \left(\frac{\omega}{c}\right)^2 \epsilon^{(1)}(\omega)\tilde{\boldsymbol{E}}(r,\theta,\omega,z) = -\frac{\omega^2}{\epsilon_0 c^2}\tilde{\boldsymbol{P}}^{\boldsymbol{NL}}(r,\theta,\omega,z). \quad (6)$$

The envelopes $\boldsymbol{A}(r,\theta,t,z)$ and $\boldsymbol{p}^{\boldsymbol{NL}}(r,\theta,t,z)$ in the frequency domain are related to $\tilde{\boldsymbol{E}}(r,\theta,\omega,z)$ and $\tilde{\boldsymbol{P}}^{\boldsymbol{NL}}(r,\theta,\omega,z)$ by [41]

$$\tilde{\boldsymbol{E}}(r,\theta,\omega,z) \simeq \tilde{\boldsymbol{A}}(r,\theta,\omega-\omega_0,z) e^{ik_0 z} \quad (7)$$

$$\tilde{\boldsymbol{P}}^{\boldsymbol{NL}}(r,\theta,\omega,z) \simeq \tilde{\boldsymbol{p}}^{\boldsymbol{NL}}(r,\theta,\omega-\omega_0,z) e^{ik_0 z}. \quad (8)$$

Introducing these expressions into equation (6)

$$\nabla^2(\tilde{\boldsymbol{A}} e^{ik_0 z}) + k(\omega)\tilde{\boldsymbol{A}} e^{ik_0 z} = -\frac{\omega^2}{\epsilon_0 c^2}\tilde{\boldsymbol{p}}^{\boldsymbol{NL}} e^{ik_0 z} \quad (9)$$

where we use $\tilde{\boldsymbol{A}}$ and $\tilde{\boldsymbol{p}}^{\boldsymbol{NL}}$ for simplicity and $k(\omega) = n_L(\omega)\omega/c$, being n_L the linear part of the refractive index. Considering that the complex amplitude $\boldsymbol{A}(r,\theta,t,z)$ evolves slowly in z over a wavelength, we can neglect the terms $\partial^2/\partial z^2$

$$\frac{\partial}{\partial z}\tilde{\boldsymbol{A}} - \frac{i}{2k_0}\left[\nabla_\perp^2 + \left(k^2(\omega) - k_0^2\right)\right]\tilde{\boldsymbol{A}} = \frac{i}{2k_0}\frac{\omega^2}{\epsilon_0 c^2}\tilde{\boldsymbol{p}}^{\boldsymbol{NL}}. \quad (10)$$

The diffraction of the beam is represented by the transverse Laplacian on the left-hand side. The nonlinear polarization term includes several contributions from second, third and higher orders, as can be seen in equation (3). Since these effects are perturbative in the range of intensities considered in this work, only the first contributions will be significant. The second-order susceptibility $\chi^{(2)}$ is responsible for second-harmonic generation, optical rectification and sum-frequency generation. However, it is nonzero only for media that lack an inversion symmetry at the molecular level. In gases, $\chi^{(2)}$ vanishes and the first nonlinear contribution to the nonlinear polarization is $\chi^{(3)}$. The third-order susceptibility $\chi^{(3)}$ is responsible for third-harmonic generation, four-wave mixing and nonlinear refraction effects, among others. Most nonlinear effects in waveguides are a consequence of the nonlinear refraction effect. In this case, the refractive index of the medium in the presence of an intense laser beam does not only depend on its frequency but also on the spatiotemporal-dependent intensity $I(r,t)$ of the laser [42] by

$$n(r,t) = n_L + n_{NL} I(r,t) \quad (11)$$

where n_L is the linear part and n_{NL} is the nonlinear part of the refractive index related to the third order susceptibility $\chi^{(3)}$. The nonlinear coefficient n_{NL} is positive in general, leading to an increase of the refractive index with the intensity of the beam.

The nonlinear polarization in the time domain for self-induced effects in waveguides becomes [43]

$$\boldsymbol{P}^{\boldsymbol{NL}}(r,\theta,t) = \epsilon_0 \chi^{(3)} \boldsymbol{E}(r,\theta,t) \int_{-\infty}^{t} R(t-\tau_1)|\boldsymbol{E}(r,\theta,\tau_1)|^2 d\tau_1. \quad (12)$$

$R(t)$ being the nonlinear response function normalized in a manner similar to the delta function, i.e. $\int_{-\infty}^{\infty} R(t)dt = 1$, and it includes the electronic and vibrational contributions. In equation (12) we consider that the electric field and the induced polarization vectors point along the same direction. We also assume that $R(t)$ obeys the causality condition $R(t) = 0$ for $t - \tau_1 < 0$, so the nonlinear polarization only depends on

the past values of the electric field. In general, the functional form of $R(t)$ can be written as

$$R(t-\tau_1) = (1-f_R)\delta(t-\tau_1) + f_R \cdot h_R(t-\tau_1) \tag{13}$$

where the first term is the instantaneous electronic response (the optical Kerr effect) and the second term is the retarded vibrational response (the stimulated Raman scattering).

2.1. Nonlinear spatial effects: self-focusing

In the case of a monochromatic laser beam, i.e. a sufficiently long laser pulse with central frequency ω_0 and a narrow spectrum, we can neglect the temporal dependence of the field since only the spatial effects are significant during the propagation in this case. In addition, we assume cylindrical symmetry, so we only take into account the spatial and longitudinal dimensions $\tilde{A}(r,\theta,\omega,z) = A(r,z)\delta(\omega)$. For the case of a material with an instantaneous third-order response, we can derive the polarization amplitude from equation (12)

$$\boldsymbol{p}^{\boldsymbol{NL}}(r,z) = 3\epsilon_0\chi^{(3)}|\boldsymbol{A}(r,z)|^2\boldsymbol{A}(r,z) \tag{14}$$

$\chi^{(3)} = 2/3 n_L n_{NL}$ being the third-order susceptibility [41] and the units of $|A(r,z)|^2$ are W cm^{-2}. Introducing this expression in equation (10)

$$\frac{\partial}{\partial z}\boldsymbol{A} - \frac{i}{2k_0(r)}\left[\nabla_\perp^2 + \left((k^R(r))^2 - k_0^2(r)\right)\right]\boldsymbol{A} + \frac{\alpha(r)}{2}\boldsymbol{A} = i\frac{\omega_0}{c}n_{NL}(r)|\boldsymbol{A}|^2\boldsymbol{A} \tag{15}$$

where $\nabla_\perp^2 = \partial^2/\partial r^2 + (1/r)\,\partial/\partial r$ and we have expressed $k(r) = k^R(r) + i\alpha(r)/2$ [44], k^R being the propagation constant, $\alpha(r)$ the linear absorption due to the gas and the propagation losses in the HCF. If the leaks are low and the absorption of the gas is negligible at the wavelengths considered here, then $k^R \gg \alpha$ and we can neglect the terms α^2 and assume that $k^R(r)/k_0(r) \approx 1$.

In equation (15) we can identify which effects change the field amplitude during the propagation. The second term on the left-hand side represents the diffraction of the pulse and the nonlinear term on the right-hand side represents the optical Kerr effect. The consequence of this nonlinear intensity-dependent term is the self-focusing of the beam towards the highest intensity regions, usually its central part. This process is activated when a laser beam with peak power above a critical value, called critical power (P_{cr}) [45], propagates through a material for which n_{NL} is positive. As a result, the medium acts as a positive lens and the beam self-focuses. This process is of great practical importance, because if the intensity of the laser beam is high enough, it can damage the material.

2.2. Nonlinear spatio-temporal effects

Since we are in a context of short pulses, we also need to study the temporal nonlinear effects in addition to the spatial effects. For this reason, we include the temporal dependence of the field amplitude and calculate the second order derivative in time of the nonlinear polarization that appears on the right-hand side of equation (2). Now the propagation constant $k(\omega) = n(\omega)\omega/c$ represents the linear response of the medium including all the dispersion terms and the absorption, being $n(\omega)$ the complex refractive index. Approximating $k(\omega)$ as a power series in $\omega - \omega_0$

$$k(\omega) = k_0(\omega_0) + k_1(\omega_0)(\omega-\omega_0) + \tilde{D}(\omega) \tag{16}$$

$$\tilde{D}(\omega) = \sum_{m\geqslant 2}^{\infty}\frac{1}{m!}k_m(\omega_0)(\omega-\omega_0)^m \tag{17}$$

where $\tilde{D}$ represents the high-order dispersion terms: $k_m(\omega_0) = [(\partial k/\partial\omega)^m]_{\omega=\omega_0}$. The first term $k_0 = k_0^R + i\alpha/2$ together with the rest k_m terms represent the complete linear dispersion response.

We can express the wave equation in the time domain introducing equations (16) and (17) into equation (9), going back to the time domain and using a frame moving with the pulse $T = t - k_1 z$ and $z' = z$.

$$\left(\frac{\partial}{\partial z} - \frac{i}{2k_0}\nabla_\perp^2\hat{T}^{-1} - iD + \frac{\alpha}{2}\right)\boldsymbol{A}(r,\theta,T,z) = \frac{ik_0}{2\epsilon_0 n_0^2}\hat{T}\boldsymbol{p}^{\boldsymbol{NL}}(r,\theta,T,z) \tag{18}$$

where we rename z' as z for simplicity. The term D is the differential operator $D(T) = \sum_{m\geqslant 2}^{\infty}(1/m!)k_m(i\partial/\partial T)^m$. The refractive index n_0 is defined as $n_0 = n_L(\omega_0)$. We have assumed that $k_0^R \approx k_0$ since the imaginary part of the refractive index is very small in our case and we can substitute the term $k_1/k_0 \approx 1/\omega_0$ ignoring the correction of the dispersion in this expression [41]. All the terms D^2, α^2 and $\partial^2/\partial z^2$ are also considered invariably small so we can neglect them. The operator $\hat{T}$ is defined as $\hat{T} = [1 + (i/\omega_0)\partial/\partial T]$. Equation (18) includes the linear effects that appear in the propagation: the diffraction, the spatio-temporal coupling (represented by $\hat{T}^{-1}$, which improves the model above the slowly varying envelope approximation) and the high-order dispersion terms through D. The spatial dynamics of the beam due to diffraction is represented by the transverse Laplacian. Related to the nonlinear dynamics, the self-steepening effect is represented by the differential operator $\hat{T}$ in the right-hand side. By considering this linear spatio-temporal coupling, we impose the slowly varying amplitude approximation in the propagation direction z, but not in time, which is useful in the case of ultrashort pulses (this approximation is known as the slowly evolving wave approximation, SEWA) [42].

It is usually stated that envelope pulse propagation description is limited to those regimes that can be described as quasi-monochromatic. However, the nonlinear envelope equation, which corresponds to equation (18) and was derived by Brabec and Krausz [44], is valid for ultrashort, broadband spectrum

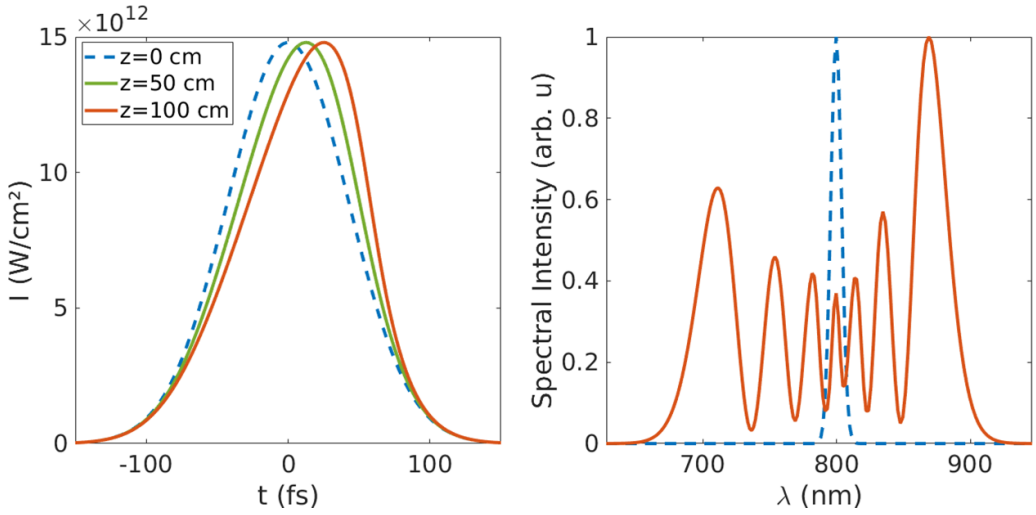

Figure 2. Self-phase modulation and self-steepening effects in a nonlinear propagation. The initial intensity and spectrum are represented in blue dashed lines.

laser pulses due to different 'correction terms' beyond the slowly varying envelope approximation. This equation can manage pulses with broad spectrum and fast temporal features, even though the field is described through its envelope.

2.2.1. Self-phase modulation and self-steepening. The subsequent step is to assume a material with purely electronic instantaneous third-order response. In that case, according to equation (12) the polarization amplitude takes the form

$$\boldsymbol{p}^{\boldsymbol{NL}}(r,\theta,t,z) = 3\epsilon_0\chi^{(3)}|\boldsymbol{A}(r,\theta,t,z)|^2\boldsymbol{A}(r,\theta,t,z) \tag{19}$$

where $\chi^{(3)} = 2/3n_L n_{NL}$ is the third-order susceptibility, so $|\boldsymbol{A}(r,\theta,t,z)|^2$ is expressed in $\mathrm{W\,cm^{-2}}$ [41]. Introducing this expression in equation (18), we obtain

$$\left(\frac{\partial}{\partial z} - \frac{i}{2k_0}\nabla_\perp^2\hat{T}^{-1} - iD + \frac{\alpha}{2}\right)\boldsymbol{A} = i\frac{\omega_0}{c}\frac{n_L n_{NL}}{n_0}\hat{T}|\boldsymbol{A}|^2\boldsymbol{A}. \tag{20}$$

The term on the right-hand side of the equation describes the self-phase modulation and self-steepening effects. Self-phase modulation is a consequence of the optical Kerr effect, the temporal analog of the self-focusing, and it also appears due to the nonlinear contribution to the refractive index, n_{NL}, which self-induces a change in the temporal phase of the pulse during the propagation and is responsible for the symmetric and modulated spectral broadening of the pulse. The operator $\hat{T}$ on the right-hand side of equation (20) describes the self-steepening effect. This effect can be understood like an intensity dependence of the group velocity, $v_g = d\omega/dk(\omega) = c/(n_L + \omega dn(\omega)/d\omega)$ [41]. In general, the nonlinear refractive index, n_{NL}, is positive and as the pulse envelope propagates with the group velocity, the peak of the pulse with high intensity slows down with respect to the wings of the pulse. As a result, the slope of the leading edge decreases while the slope of the trailing edge becomes steeper, which can lead to an optical shock wave. This temporal asymmetry induced by the self-steepening leads to an asymmetry in the spectrum. Since the slope is higher in the trailing edge of the pulse, there is a larger spectral broadening in the blue side of the spectrum, as figure 2 illustrates.

2.2.2. Delayed Raman response. If we now assume a material with molecular response, which is slower than the electronic response, we have to consider the non-instantaneous response of the third-order susceptibility. Taking this into account, the Kerr term has an instantaneous part and a delayed part. We have to use the general form of the nonlinear polarization, as defined in equation (12) [43] and the polarization amplitude takes the form

$$\boldsymbol{p}^{\boldsymbol{NL}}(r,\theta,t,z) = 3\epsilon_0\chi^{(3)}\boldsymbol{A}(r,\theta,t,z) \times \int_{-\infty}^{t} R(t-\tau_1)|\boldsymbol{A}(r,\theta,\tau_1,z)|^2 d\tau_1. \tag{21}$$

Introducing this expression in equation (18)

$$\left(\frac{\partial}{\partial z} - \frac{i}{2k_0}\nabla_\perp^2\hat{T}^{-1} - iD + \frac{\alpha}{2}\right)\boldsymbol{A} = i\frac{\omega_0}{c}\frac{n_L n_{NL}}{n_0}\hat{T}\boldsymbol{A}\int_{-\infty}^{T} R(T-\tau_1)|\boldsymbol{A}(\tau_1)|^2 d\tau_1. \tag{22}$$

The terms on the left-hand side of equation (22) are the diffraction, the space-time coupling, the dispersion and the linear absorption. On the right-hand side, we describe together the self-phase modulation and the Raman delayed response, both affected by self-steepening.

In the particular case of gases, the complete nonlinear temporal response can be expressed as $R(T-t) = (1-f_R)\delta(T-t) + f_R/\tau_K \cdot \exp[-(T-t)/\tau_K]$, f_R being the ratio between the self-phase modulation and the Raman effect, and τ_K the characteristic time for the Raman response [8]. Because of the delayed Raman response, the pulse spectrum suffers a red shift

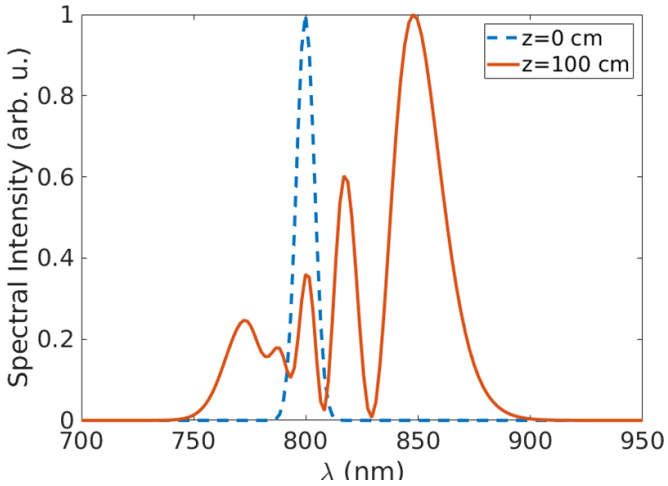

Figure 3. Pulse spectrum modulated by the Raman response when propagating through air.

as the pulse propagates inside the HCF (see figure 3). This is due to the fact that Raman effect is the result of light interaction with the vibrations of the molecules.

The Raman scattering is an inelastic scattering process in which a medium absorbs a photon and emits a new one with slightly different frequency. Usually, the frequency of the emitted photon is lower than the frequency of the one absorbed. The energy difference is accounted for by a vibrational energy (see figure 4). When this process is stimulated by the light intensity, it can be described as a nonlinear third order process in a similar way as the optical Kerr effect, as we have presented. The new lower frequencies components, generated from the ground level, are called the Raman Stokes components. There are also Raman anti-Stokes components, which consist of transitions from an excited level to the ground level, but they are much weaker than the Stokes components. Of course, if the intensity of the Raman Stokes component is large enough, the re-emitted photon can be scattered again at a lower energy, and so on, which means that the process can cascade generating a broadband spectrum at longer wavelengths.

2.2.3. Ionization effects: plasma generation and multiphoton absorption. When the intensity of the pulse reaches 10^{13}–$10^{14}\,\mathrm{W\,cm^{-2}}$, it can ionize the molecules or atoms of the medium filling the core of the HCF. These intensity values can be reached, for example, when the pulse propagates inside the HCF and self-focuses, leading to the ionization of the medium and the generation of plasma. The way of introducing the effects of the ionization in the previous equations is by means of the plasma current density, J_p, associated with the ionized medium [46, 47].

$$\boldsymbol{\nabla^2 E} - \frac{1}{c^2}\frac{\partial^2 \boldsymbol{E}}{\partial t^2} = \frac{1}{\epsilon_0 c^2}\left(\frac{\partial^2}{\partial t^2}\boldsymbol{P^L} + \frac{\partial^2}{\partial t^2}\boldsymbol{P^{NL}} + \frac{\partial \boldsymbol{J_p}}{\partial t}\right) \tag{23}$$

$$\frac{\partial \boldsymbol{J_p}}{\partial t} = -\frac{\sigma}{2}(1+i\omega_0\tau_c)\rho\boldsymbol{E} - \frac{W(|\boldsymbol{E}|^2)U_i}{2I}(\rho_{at}-\rho)\boldsymbol{E} \tag{24}$$

where U_i is the ionization potential of the gas, $\rho(r,\theta,t,z)$ is the density of ionized electrons, ρ_{at} is the atomic density of the medium, τ_c is the collision time (relaxation time) and σ is the cross-section for the inverse Bremsstrahlung, which is written as follows

$$\sigma = \frac{\omega_0}{n_L(\omega)c\rho_c}\frac{\omega_0\tau_c}{1+\omega_0^2\tau_c^2}. \tag{25}$$

$\rho_c = \epsilon_0 m_e\omega_0^2/e^2$ being the value of the critical plasma density above which the plasma becomes opaque for the frequency ω_0, and m_e and e are the electron mass and charge, respectively. The first term of equation (24) is the change in the refractive index induced by the presence of the ionized electrons. The real part of this first term represents the absorption of light by the generated plasma itself, while the imaginary part leads to plasma defocusing and blue shifting of the laser spectrum, typically observed in ionized gases [48]. The second term accounts for the absorption related to the ionization process. The parameter $W(|E|^2)$ is the ionization rate, which depends on U_i, the laser intensity and ω_0. We use the model of Perelomov–Popov–Terent'ev (PPT model) to calculate the ionization rates since it is valid for a wider intensity range compared to other ionization models and it is able to describe the ionization both in the multiphoton regime, ($I \ll 10^{13}\,\mathrm{W\,cm^{-2}}$), and the tunnel regime, ($I \gg 10^{14}\,\mathrm{W\,cm^{-2}}$), [42, 49, 50]. Both plasma defocusing and absorption prevent beam collapse when self-focusing dominates the propagation.

Including these terms, the nonlinear wave equation for ultrashort pulses is the following

$$\left(\frac{\partial}{\partial z} - \frac{i}{2k_0}\nabla_\perp^2\hat{T}^{-1} - iD + \frac{\alpha}{2}\right)\boldsymbol{A} = N(|A|^2, A, \rho) \tag{26}$$

where the nonlinear effects mentioned above are included in

$$N(|A|^2,A,\rho) = N_{Kerr}(|A|^2,A) + N_{ioniz}(A,\rho) + N_{abs}(|A|^2,A,\rho) \tag{27}$$

$$N_{Kerr}(|A|^2,A) = i\frac{\omega_0}{c}\frac{n_L n_{NL}}{n_0}\hat{T}\left(\int_{-\infty}^{T} R(T-\tau_1)|\boldsymbol{A}(\tau_1)|^2 d\tau_1\right)\boldsymbol{A} \tag{28}$$

$$N_{ioniz}(A,\rho) = -i\frac{\sigma}{2}\omega_0\tau_c\hat{T}^{-1}\rho\boldsymbol{A} \tag{29}$$

$$N_{abs}(|A|^2,A,\rho) = -\frac{W(|\boldsymbol{A}|^2)U_i}{2|\boldsymbol{A}|^2}(\rho_{at}-\rho)\boldsymbol{A} - \frac{\sigma}{2}\hat{T}^{-1}\rho\boldsymbol{A}. \tag{30}$$

Equation (26) is solved simultaneously with the equation describing the evolution of the density of electrons, where we assume that the avalanche ionization and the plasma recombination processes are negligible

$$\frac{\partial \rho}{\partial t} = W(|A|^2)(\rho_{at}-\rho). \tag{31}$$

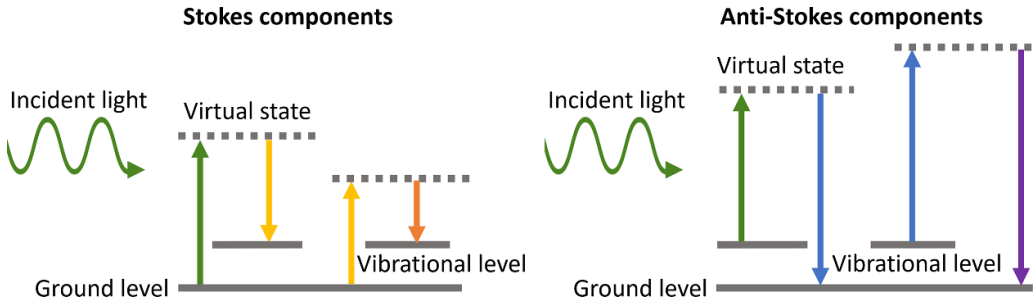

Figure 4. Left panel: an incident photon (green) can be absorbed by the nonlinear medium and scattered with lower energy (Stokes components (yellow and orange)). Right panel: an incident photon (green) can be absorbed by the nonlinear medium and scattered with higher energy (anti-Stokes components (blue and purple)). In the process, there is a molecular transition between different energy states.

2.3. HCF spatial modes

In this subsection, we will introduce the most common spatial modes of the HCF used to study the propagation of a laser pulse. We consider a dielectric and cylindrical HCF and we assume that if the wavelength is smaller than the core radius ($\lambda \ll r_F$) and the HCF does not present curvature, the light propagates essentially within the core by grazing incidence reflections against the wall, so there is little energy flux into the cladding due to refraction [51]. The field in the cladding is weak, and the index difference between the core and the cladding is high enough that any coupling on the femtosecond timescale from the cladding back to the core is negligible, as done in previous works [52]. We also assume that $|k_z/k - 1| \ll 1$, which means that the axial propagation constant of each mode, k_z, is nearly equal to that of free space, so only modes with low losses are supported.

There are three types of spatial modes supported by this cylindrical HCF: transverse circular electric modes, transverse circular magnetic modes and hybrid modes. We will distinguish between different spatial modes with two integers, p and q. The value $|p|$ is the number of periods of each field component in the azimuthal direction and q is the number of maxima and minima of each field component in the radial direction. The approximate expression of the electric field for the different spatial modes in the core of the HCF can be written as follows

2.3.1. Circular electric modes TE_{0q}, ($p = 0$).

If $(E_{0q})_z = 0$ and $(E_{0q})_r = 0$ everywhere, the electric field has only an azimuthal component $(E_{0q})_\theta$ that can be approximately expressed as

$$(E_{0q})_\theta = J_1\left(u_{0q}\frac{r}{r_F}\right) \tag{32}$$

where u_{0q} is the qth root of the Bessel function of the first kind J_1 and r_F is the core radius of the HCF. The Bessel function of the first kind J_n is generally defined as $J_n(x) = 1/\pi \int_0^\pi \cos(n\tau - x\sin\tau)d\tau = 1/2\pi \int_{-\pi}^{\pi} \exp(i(n\tau - x\sin\tau))\,d\tau$.

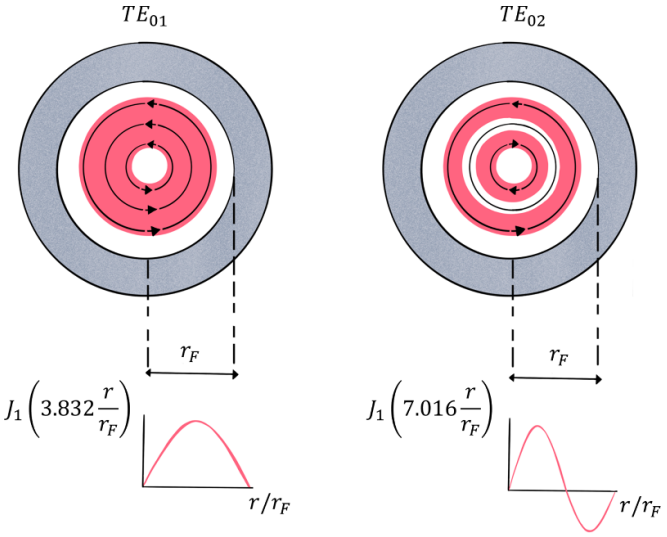

Figure 5. First two circular electric modes TE_{01} and TE_{02}.

The result is a transverse circular electric mode (TE_{0q}, $q = 1, 2, \ldots$) in which the electric field lines are transverse concentric circumferences centred on the propagation axis. These spatial modes, which belong to the so-called vector beam family of the optical beams, present azimuthal polarization and a singularity in the propagation axis. As a consequence of this spatially varying polarization, the spatial intensity distribution has a ring-shape profile. A simple representation of the first two spatial modes of the family, TE_{01} and TE_{02} modes, is shown in figure 5, where vectors represent the polarization direction of the local field.

2.3.2. Circular magnetic modes TM_{0q}, ($p = 0$).

If $(E_{0q})_\theta = 0$ everywhere, the other components of the electric field can be approximately expressed as

$$(E_{0q})_r = J_1\left(u_{0q}\frac{r}{r_F}\right) \tag{33}$$

where u_{0q} is the qth root of the Bessel function of the first kind J_1. The longitudinal component of these modes, $(E_{0q})_z$, is very small if $\lambda \ll r_F$ and we can neglect it. The result is a transverse

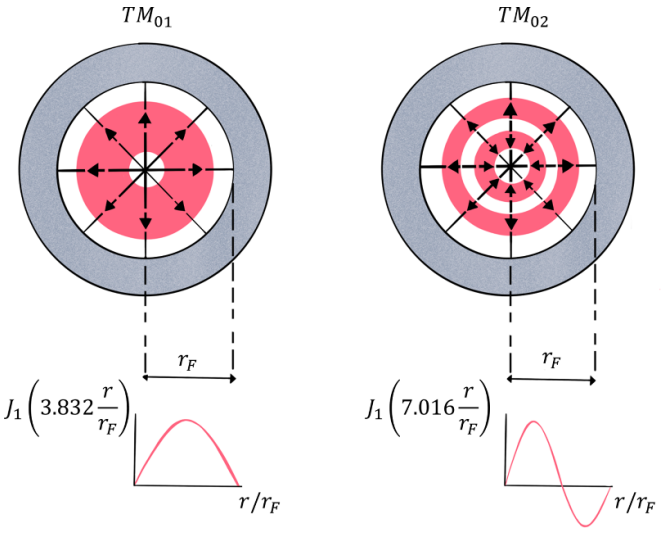

Figure 6. First two circular magnetic modes TM_{01} and TM_{02}.

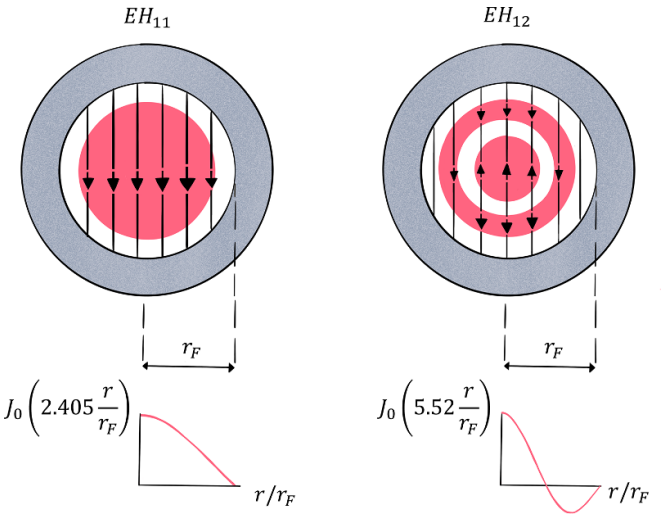

Figure 7. First two hybrid modes EH_{11} and EH_{12}.

circular magnetic mode (TM_{0q}, $q = 1, 2, \ldots$) in which the electric field lines are radial lines [51]. These spatial modes, also named vector beams as the TE_{0q} modes, present radial polarization and a singularity in the propagation axis. As the TE_{0q} modes, the spatial intensity distribution of the circular magnetic modes has a ring-shape profile (see figure 6).

2.3.3. Hybrid modes EH_{pq} ($p \neq 0$). In this case, the approximated expressions for each field component are

$$(E_{pq})_\theta = J_{p-1}\left(u_{pq}\frac{r}{r_F}\right)\cos(p\theta) \tag{34}$$

$$(E_{pq})_r = J_{p-1}\left(u_{pq}\frac{r}{r_F}\right)\sin(p\theta) \tag{35}$$

where we have neglected the longitudinal component of these modes, $(E_{pq})_z$, for the same reason as in TM modes. In equations (34) and (35), u_{pq} is the qth root of the Bessel function of the first kind J_{p-1}.

The most interesting modes of this type for the propagation inside the HCF are the EH_{1q} modes, as they present a uniform linear polarization and a maximum of intensity on the propagation axis. In the case of the higher-order modes ($q > 1$), they present concentric intensity rings. A simple scheme of the first two spatial modes of these EH_{1q} modes, EH_{11} and EH_{12} is shown in figure 7. Among the hybrid modes of the first order, EH_{11} mode is called the fundamental spatial mode [51] and it is the most frequently used in standard post-compression setups.

2.3.4. Necklace beams. These spatial modes are a composition of two degenerate hybrid modes: $EH_{(-|p|)q} + EH_{(|p|+2)q}$, both with the same complex propagation coefficient. If these two hybrid modes are combined, we obtain a new family of linearly polarized modes [51] represented by

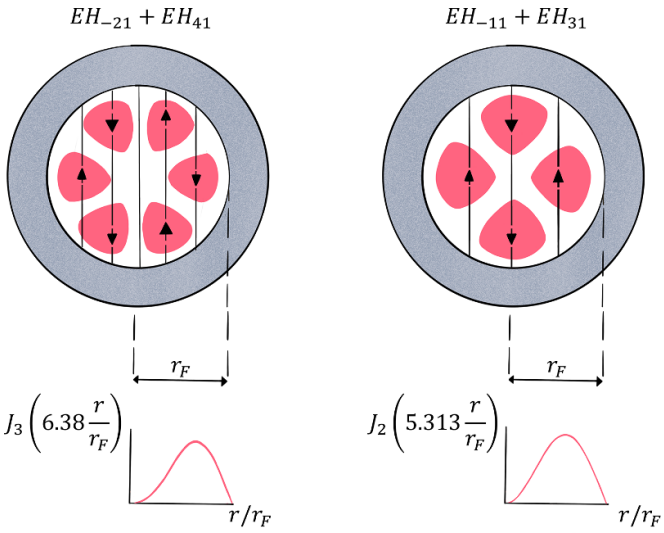

Figure 8. Two necklace type modes with 6 and 4 beads or lobes.

$$EH_{(-|p|)q} + EH_{(|p|+2)q} = J_{p+1}\left(u_{(p+2)q}\frac{r}{r_F}\right)\sin[(p+1)\theta] \tag{36}$$

where $u_{(p+2)q}$ is the qth root of the Bessel function of the first kind J_{p+1}. Necklace beams are a type of structured laser beams with amplitude and phase rotational symmetry around the propagation axis. There are different families of necklace beams in a HCF depending on the number of rings and beads they present (see figure 8).

2.3.5. Propagation and absorption coefficients. The propagation and absorption coefficients of the spatial modes of the HCF presented before, are the real and imaginary parts of the axial complex propagation coefficient k_z [45]

$$k_z(\omega) = \beta_{pq}(\omega) + i\alpha_{pq}(\omega). \tag{37}$$

The expressions for β_{pq} and α_{pq} are the following:

$$\beta_{pq}(\omega) = n_L(\omega)\frac{2\pi}{\lambda}\left[1 - \frac{1}{2}\left(\frac{u_{pq}\lambda}{2\pi r_F n_L(\omega)}\right)^2\right] \tag{38}$$

$$\alpha_{pq}(\omega) = \left(\frac{u_{pq}}{2\pi}\right)^2 \frac{\lambda^2}{n_L(\omega)^2 r_F^3}\nu_p \tag{39}$$

where $n_L(\omega)$ is the linear refractive index of the medium in the core and λ is the central wavelength in vacuum. The expression for ν_p depends on the chosen spatial mode:

$$\nu_p = \begin{cases} \left(\nu^2 - 1\right)^{-1/2} & TE_{0q} \\ \nu^2\left(\nu^2 - 1\right)^{-1/2} & TM_{0q} \\ \frac{1}{2}\left(\nu^2 + 1\right)\left(\nu^2 - 1\right)^{-1/2} & EH_{pq} \end{cases} \tag{40}$$

where ν is the ratio between the refractive index of the cladding and the core. Theequations (38) and (39) can be used as the propagation constant k^R and the absorption coefficient α defined in the wave equations above.

Special attention should be paid to the expression of β_{pq} in equation (38). An important topic in nonlinear pulse compression is the dispersion experienced by laser pulses during the propagation inside the gas-filled HCF. We can notice that selecting carefully the pulse wavelength, the core radius or the spatial modes coupled into the HCF, the group velocity dispersion can be negative ($\partial^2\beta_{pq}/\partial\omega^2 < 0$), thus entering into the anomalous dispersion regime. In this anomalous dispersion region, new features arise from the interplay between the second order dispersion (or group velocity dispersion) and self-phase modulation. These two effects can cooperate in such a way that the pulse propagates as an optical soliton and it can self-compress during the propagation.

On the other hand, the attenuation constant α is proportional to $\lambda^2/{r_F}^3$. This allows us to decrease the losses by choosing large core radii, but at the same time, this will reduce the negative contribution of β_{pq} and enhance the multimode propagation regime. We can see from the expression for α_{pq} that high-order modes present higher losses.

3. Numerical methods

The nonlinear partial differential equation (NPDE) (18) is hard to solve analytically in most of the cases, and a numerical solution of the nonlinear propagation equation is necessary to understand the nonlinear effects that affect the propagation of the pulse. Although there are different methods to obtain the exact analytical solution of NPDEs [53–56], in the frame of this work a numerical approach of this solution is enough to simulate the dynamics observed in the experiments. We have developed different numerical models according to the effects that we are interested in or to the symmetry of the spatial profile of the input beam. Several numerical methods can be used to solve the nonlinear propagation equation. The easiest one to implement is a split-step scheme in which the linear terms (diffraction, dispersion and absorption) and the nonlinear terms are solved separately [43]. Although in general, diffraction, dispersion and nonlinearity act together through the propagation along the HCF, with the split-step method we can obtain an approximate solution by assuming that linear and nonlinear effects act independently in a small longitudinal step size. To solve the linear and nonlinear part, we use a variety of numerical models like finite-difference scheme, Fourier space or Runge-Kutta algorithm.

3.1. The time-independent model (1 + 1)D

The first numerical model we have developed is time-independent, useful for the understanding of the self-focusing dynamics in HCF, which is a purely spatial effect. In the literature, the early numerical studies on the self-focusing dynamics solved a propagation equation including only the diffraction and self-focusing effects and neglecting any time-dependent term [57]. In accordance with this approach, we have developed a time-independent model, (1 + 1)D model, based on the nonlinear propagation equation (15) to study the spatial dynamics of a monochromatic laser beam inside the HCF and how the spatial confinement influences the nonlinear propagation dynamics. The notation (1 + 1)D refers to the fact that we only take into account the radial transverse dimension r plus the propagation dimension z. We assume linear polarization so the envelope is a scalar quantity $A(r,z)$.

In equation (15), the linear absorption of the spatial mode propagating inside the HCF is $\alpha(r) = 2\alpha_{pq}(r)$, defined in equation (39). Both refractive indices, n_L and n_{NL}, show radial dependence since we are including the optical linear and nonlinear response of the core and the cladding of the HCF. The amplitude of the laser beam $A(r,z)$ has initially, at $z = 0$, the radial dependence of a HCF spatial mode, so it can be expressed as $A(r,0) = F(r)$, $F(r)$ being the modal field distribution. The intensity $|A(r,z)|^2$ has units of $\mathrm{W\,cm^{-2}}$ so that the product $n_{NL}(r)|A(r,z)|^2$ is dimensionless. Equation (15) is solved numerically using a standard split-step method. To understand this method, we write equation (15) in the form of the two terms that govern the beam propagation, $\hat{L}$ and $\hat{N}$.

$$\frac{\partial A(r,z)}{\partial z} = \hat{L}A(r,z) + \hat{N}(|A|^2, A). \tag{41}$$

The linear part of the propagation equation, $\hat{L}$, represents the diffraction and the absorption of the input spatial mode propagating inside the HCF. The nonlinear part, $\hat{N}$, represents the self-focusing process induced by the optical Kerr effect on the propagation [49]. With the split-step method we solve equation (41) in two steps. In the first step, the linear operator $\hat{L}$ is discretized with a finite-difference scheme for the derivatives in z and r. The resulting system of equations is solved using a Crank–Nicolson algorithm [49].

$$\frac{\partial A}{\partial z} = F\left(A, r, z, \frac{\partial A}{\partial r}, \frac{\partial^2 A}{\partial r^2}\right) \tag{42}$$

$$\frac{\bar{A}_i^{j+1} - A_i^j}{\Delta z} = \frac{1}{2}\left(F_i^{j+1} + F^j{}_i\right) \tag{43}$$

where the i subscript refers to the radial points in the grid and the j superscript refers to the longitudinal points in the propagation direction. The equation for the Crank–Nicolson method is a combination of the forward difference at the point j and the backward difference at point $j+1$ for the longitudinal coordinate. With this algorithm we solve the unknown envelope at the point $j+1$, $\bar{A}_i^{j+1}$, only including the linear effects. Discretizing the equation above, we obtain a matrix equation of the form

$$B\bar{A}^{j+1} = CA^{j} \tag{44}$$

where B and C are both tridiagonal matrices. We use Neumann boundary conditions in $r=0$, $\partial A/\partial r = 0$, and since there is a singularity in $r=0$, we apply L'Hôpital's rule

$$\lim_{r\to 0}\left(\frac{1}{r}\frac{\partial A}{\partial r}\right)_{r=0} = \frac{\partial^2 A}{\partial r^2}. \tag{45}$$

Moreover, we implemented an absorber at the end of the radial grid to avoid reflections [58]. Thus, the matrices B and C are the following

$$B = \begin{pmatrix} 1+4a-a\xi & -4a & 0 & \dots & 0 \\ -a(1-\frac{\Delta r}{2r}) & 1+2a-a\xi & -a(1+\frac{\Delta r}{2r}) & \dots & 0 \\ \vdots & \vdots & \ddots & \dots & \vdots \\ 0 & 0 & \dots & -a(1-\frac{\Delta r}{2r}) & 1+2a-a\xi \end{pmatrix} \tag{46}$$

$$C = \begin{pmatrix} 1-4a+a\xi & 4a & 0 & \dots & 0 \\ a(1-\frac{\Delta r}{2r}) & 1-2a+a\xi & a(1+\frac{\Delta r}{2r}) & \dots & 0 \\ \vdots & \vdots & \ddots & \dots & \vdots \\ 0 & 0 & \dots & a(1-\frac{\Delta r}{2r}) & 1-2a+a\xi \end{pmatrix} \tag{47}$$

where $a = i\Delta z/4k_0\Delta r^2$ and $\xi = \Delta r^2\left[(k^R)^2 - k_0^2\right]$, Δz and Δr being the longitudinal and radial step sizes, respectively. We have approximated the derivatives in the transverse Laplacian with a finite-difference method, with the forward difference in z and the centred difference in r.

In the second step, the nonlinearity acts individually and it is solved as an exponential operator $\exp(\Delta z\hat{N})$, which means introducing an intensity-dependent phase factor $i(\omega_0/c)n_{NL}|A|^2$.

$$\frac{\partial A}{\partial z} = i\frac{\omega_0}{c}n_{NL}|A|^2 A \tag{48}$$

$$A^{j+1} = \exp\left(i\frac{\omega_0}{c}n_{NL}\left|\bar{A}^{j+1}\right|^2\Delta z\right)\bar{A}^{j+1}. \tag{49}$$

$\bar{A}^{j+1}$ being the solution obtained when solving linear part with the Crank–Nicolson algorithm. This model can simulate the spatial dynamics of the pulse propagating inside the HCF.

3.2. The time-dependent model (2 + 1)D

Since HCFs are multimode systems, it is not surprising that their multimode nature could be relevant to fully understand the pulse dynamics during the propagation inside the HCF. In the (1 + 1)D model the diffraction is modelled solving the transverse Laplacian, so we do not take into account the full dynamics of the different spatial modes, since this model does not consider that each mode propagates differently. However, if the pulse intensity is sufficiently high, the nonlinear propagation through the HCF induces an important energy transfer between different spatial modes [52]. In addition, considering the short pulse duration of the laser beams, the dispersion and nonlinear temporal effects could also play a significant role in the propagation. For this reason, a numerical model that includes the temporal dynamics is needed and instead of solving the radial effects directly, this model decomposes the electric field into the spatial modes considering only the spatial structure in the core of the HCF. Since these are leaky modes, the propagation losses of each mode are also included in the model.

The time-dependent model, (2 + 1)D model, includes the spatial and temporal dynamics of the pulse. We refer to this model as (2 + 1)D model, meaning two dimensions, the radial r and the temporal T dimensions, plus the propagation dimension z. We assume linear polarization so the envelope is a scalar quantity $A(r,T,z)$. Considering cylindrical symmetry again, the propagation equation for the temporal envelope of the pulse, $A(r,T,z)$, is the one obtained in equation (26), where we include the spatio-temporal dynamics and the effects related to the ionization of the gas filling the HCF. Since we are considering only the propagation in the core, now n_L and n_{NL}, the linear and nonlinear refractive indices of the gas filling the HCF, do not show radial dependence as before. Once more, we write equation (26) in the form of the two terms that govern the beam propagation, $\hat{L}$ and $\hat{N}$.

$$\frac{\partial A(r,T,z)}{\partial z} = \hat{L}A(r,T,z) + \hat{N}(|A|^2, A, \rho) \tag{50}$$

where $A(r,T,z)$ can be expressed initially as $A(r,T,0) = F(r)\exp\left(-T^2/T_0^2\right)$, $F(r)$ being the initial modal field distribution. Equation (50) is solved again with a split-step method, as is described in detail in [8]. In this case, the linear part is solved decomposing the input pulse in the family of spatial modes of the HCF, and the nonlinear part is solved by means of a fourth-order Runge-Kutta algorithm in the time domain. The nonlinear operator includes self-focusing, self-phase modulation, self-steepening, Raman, ionization and the losses due to the ionization process and plasma absorption. The model uses a finite number of modes, N, for the modal decomposition, usually 30, which are enough to model the beam dynamics.

To solve the linear part we start from the premise that we already know the pulse envelope $A(r,T,z)$ in a certain point but our goal is to obtain $A(r,T,z+\Delta z)$. The envelope can always be expressed as the combination of different spatial modes in the Fourier domain

$$\tilde{A}(r,\omega,z) = \sum_{q=1}^{N} c_{pq}(\omega,z)F_{pq}(r) \tag{51}$$

where $\tilde{A}(r,\omega,z)$ represents the Fourier Transform of $A(r,T,z)$ and $F_{pq}(r)$ is the family of pq-spatial modes propagating inside the HCF (the modes TE_{0q}, TM_{0q} and EH_{pq} with $q = 1,2,3\ldots$). The coefficients of the decomposition, c_{pq}, are calculated by doing the inverse Hankel Transform of the spatial beam distribution in the core of the HCF [59].

$$c_{pq}(\omega,z) = \frac{1}{r_F^2 J_p^2(u_{pq})}\int_0^{r_F} \tilde{A}(r,\omega,z)J_{p-1}\left(u_{pq}\frac{r}{r_F}\right)rdr \tag{52}$$

where u_{pq} are the qth-zeros of the J_{p-1} Bessel function of the first kind of order $p-1$.

In the first part of the equation (50) the operator $\hat{L}$ represents the linear propagation effects: diffraction, absorption and also dispersion, that we solve using the propagation and absorption coefficients of each mode, $\beta_{pq}(\omega)$ and $\alpha_{pq}(\omega)$ in the frequency domain.

$$A(r,\omega,z+\Delta z) = \sum_{q=1}^{N} c_{pq}(\omega,z)F_{pq}(r)exp \times \left[i\left(\beta_{pq}(\omega) + i\alpha_{pq}(\omega)\right)\Delta z\right]. \tag{53}$$

In this case, the spatio-temporal coupling is included in the propagation constant of each mode $\beta_{pq}(\omega)$, as a correction to the dispersion relation $k(\omega)$ in free space [60].

The nonlinear part, $\hat{N}$, not only includes self-focusing but also self-phase modulation, self-steepening, Raman, the ionization and all the losses related to it. The analytical expression that we use for each nonlinear term is standard and can be found in equations (28)–(30). Equation (26) is solved simultaneously with the evolution of the density of electrons in equation (31). At each step in the propagation direction, z, the ionization is calculated based in the intensity at that step and introduce in the nonlinear operator $\hat{N}$. To solve the nonlinear operator, we use a fourth-order Runge-Kutta algorithm in the time domain. The evolution of the free-electron density is also solved with a fourth-order Runge-Kutta method, using the rates obtained from the PPT model.

This model simulates the complete spatiotemporal dynamics of the pulse propagating inside the HCF. We could simplify it ignoring the spatial dynamics to study only the temporal effects with a (1 + 1)D model in time. In this case the input field can be expressed as $A(T,0) = A_0\exp\left(-T^2/T_0^2\right)$. We will use this time-dependent (1 + 1)D model in section 4 to study the DW emission in HCFs.

3.3. The non-cylindrical symmetry model (3 + 1)D

In the case of nonlinear propagation of laser beams without cylindrical symmetry, such as necklace beams, we need to modify the previous models to include the azimuthal dependence in the spatio-temporal dynamics. We have developed a three-dimensional (3 + 1)D model, that includes the two transverse dimensions (radial r and azimuthal θ) and the temporal dimension T, plus the propagation dimension z. We assume linear polarization so the envelope is a scalar quantity $A(r,\theta,T,z)$. The propagation equation for the envelope of the pulse in cylindrical coordinates, $A(r,\theta,T,z)$, is again equation (26) but including now the azimuthal coordinate, which means that the transverse Laplacian is expressed now as $\nabla_\perp^2 = \partial^2/\partial r^2 + (1/r)\,\partial/\partial r + \left(1/r^2\right)\partial^2/\partial\theta^2$. As the previous models, this equation is also solved with a split-step method.

$$\frac{\partial A(r,\theta,T,z)}{\partial z} = \hat{L}A(r,\theta,T,z) + \hat{N}(|A|^2,A,\rho) \tag{54}$$

where $A(r,\theta,T,z)$ can be expressed initially as $A(r,\theta,T,0) = F(r,\theta)\exp\left(-T^2/T_0^2\right)$, $F(r,\theta)$ being the initial modal field distribution. The first term, $\hat{L}$, represents the linear effects, namely the diffraction, the linear losses and the dispersion of the laser beam in the HCF. The expression that we have used for these effects in this case is:

$$\hat{L} = \frac{i}{2k_0}\left(\frac{\partial^2}{\partial r^2} + \frac{1}{r}\frac{\partial}{\partial r} + \frac{1}{r^2}\frac{\partial^2}{\partial\theta^2}\right)\hat{T}^{-1} - \frac{\alpha}{2} + \sum_{m\geqslant 2}^{\infty}\frac{i^{m+1}}{m!}k_m\frac{\partial^m}{\partial T^m} \tag{55}$$

where $k_0 = n_0\omega_0/c$ and n_0 is the linear refractive index at ω_0, $\alpha = 2\alpha_{pq}$ is the absorption coefficient of the input spatial mode and $k_m = \left(\partial^m k/\partial\omega^m\right)_{\omega_0}$, $k(\omega) = n_L(\omega)\omega/c$ being the dispersion relation of the gas, where $n_L(\omega)$ is represented by the corresponding Sellmeier equation.

The second term, $\hat{N}$, represents the most significant nonlinear effects. The expressions that we have used for these effects are the same we use in the (2 + 1)D model. This model is a 3D extension of the (2 + 1)D model, enhanced to study the nonlinear propagation of beams without cylindrical symmetry through gas-filled HCFs.

We solve equation (54) by using a split-step method again. Although it is possible to perform a mode decomposition for beams without cylindrical symmetry, it is quite time-consuming since we should consider spatial modes from different families and the coupling between them. Hence, it is more convenient to directly solve the Laplacian operator

including the spatiotemporal coupling. We solve the linear part at different steps, the dispersion is solved as an exponential operator evaluated in the Fourier domain using the fast Fourier transform (FFT) algorithm.

$$\tilde{A}(r,\theta,\omega,z+\Delta z)=\exp\left(\Delta z k(\omega)\right)\tilde{A}(r,\theta,\omega,z). \tag{56}$$

The evaluation of equation (56) is straightforward and relatively fast using FFT algorithm. The azimuthal dependence is solved also in the Fourier space, which involves replacing the differential operator $\partial^2/\partial\theta^2$ by $-l^2$, where l is the orbital angular momentum. The diffraction term in equation (55) is then $i/2k_0\cdot\left[\partial^2/\partial r^2+(1/r)\,\partial/\partial r-l^2/r^2\right]\hat{T}^{-1}$ and it can be solved now using a Crank–Nicolson algorithm, as in the (1 + 1)D model, applied to each spectral component, which allow us to consider also the spatio-temporal coupling effect. The matrix equation has the same form as in equation (44). Since the azimuthal term presents another singularity at $r=0$, we avoid this point and start the simulation in $\Delta r/2$. We apply again the Neumann boundary conditions on axis, so $(\partial A/\partial r)_{r=0}=0$. In this (3 + 1)D model we only simulate the propagation in the core of the HCF assuming that the light is confined inside the core and it does not escape into the cladding, so we apply the Dirichlet boundary condition at the core edge, where $A=0$ if $r=r_F$. The matrices B and C are the following

$$B=\begin{pmatrix} 1+a(1+\Delta r^2\frac{l^2}{r^2}+\frac{\Delta r}{2r}) & -a(1+\frac{\Delta r}{2r}) & 0 & \dots & 0\\ -a(1-\frac{\Delta r}{2r}) & 1+2a+a\Delta r^2\frac{l^2}{r^2} & -a(1+\frac{\Delta r}{2r}) & \dots & 0\\ \vdots & \vdots & \ddots & \dots & \vdots\\ 0 & 0 & \dots & 0 & 1 \end{pmatrix} \tag{57}$$

$$C=\begin{pmatrix} 1-a(1+\Delta r^2\frac{l^2}{r^2}+\frac{\Delta r}{2r}) & a(1+\frac{\Delta r}{2r}) & 0 & \dots & 0\\ a(1-\frac{\Delta r}{2r}) & 1-2a-a\Delta r^2\frac{l^2}{r^2} & a(1+\frac{\Delta r}{2r}) & \dots & 0\\ \vdots & \vdots & \ddots & \dots & \vdots\\ 0 & 0 & \dots & 0 & 0 \end{pmatrix} \tag{58}$$

where $a=\left(i\Delta z/4k_0\Delta r^2\right)\left(1+\omega/\omega_0\right)^{-1}$. The step sizes in the longitudinal and radial dimensions are Δz and Δr, respectively. We have included the angular momentum obtained from the Fourier transform of the azimuthal coordinate in the diagonal terms.

The rest of the terms that appear in equation (26) included in the nonlinear part, are solved with a fourth-order Runge-Kutta algorithm in the time domain as in the (2 + 1)D model.

4. Application of the numerical model

With the numerical models presented above, it is possible to simulate the propagation of a laser pulse through the HCF in different scenarios. In this case, we are going to show the application of the model to study a particular situation, the self-compression of the pulse in the propagation and the subsequent DW generation.

4.1. DW emission in HCFs

The dispersion in the HCF is calculated from the propagation coefficient $\beta_{pq}(\omega)$ of each spatial mode, defined in equation (38), and it depends on the gas pressure through the linear refractive index of the gas. The DW emission consists of an energy transfer to a certain frequency, which lies in the normal dispersion regime, produced under perfect phase-matching conditions. This phase-matching condition depends on the propagation constants of the soliton and the DW, β_{sol} and β_{DW} respectively. While the soliton propagates nonlinearly in the anomalous dispersion region, the DW propagates linearly in the normal dispersion region:

$$\Delta\beta=\beta_{DW}(\omega)-\beta_{sol}(\omega)=0 \tag{59}$$

$$\beta_{sol}(\omega)=\beta_{pq}(\omega_{sol})+\left(\beta_{pq}(\omega_{sol})\right)_1(\omega-\omega_{sol})+\frac{\omega_{sol}n_{NL}I_{sol}}{2c} \tag{60}$$

$$\beta_{DW}(\omega)\approx\beta_{pq}(\omega_{sol})+\left(\beta_{pq}(\omega_{sol})\right)_1(\omega-\omega_{sol})+\tilde{D}(\omega) \tag{61}$$

where we have considered that the soliton and the DW propagate as the pq-spatial mode of the HCF, however, the DW emission can occur also from different spatial modes. Subscripts indicate frequency derivatives and $\tilde{D}(\omega)$ denotes the higher-order dispersion terms, as defined in equation (17). The parameter I_{sol} is the self-compressed peak intensity and ω_{sol} is the soliton frequency.

One important parameter is the zero dispersion wavelength (ZDW), which is the wavelength at which the HCF group velocity dispersion is zero $(\partial^2\beta_{pq}/\partial\omega^2)_{\omega_{ZD}}=0$. The dispersion that the pulse experiences is anomalous for pulse wavelengths longer than the ZDW, and normal for shorter wavelengths. In

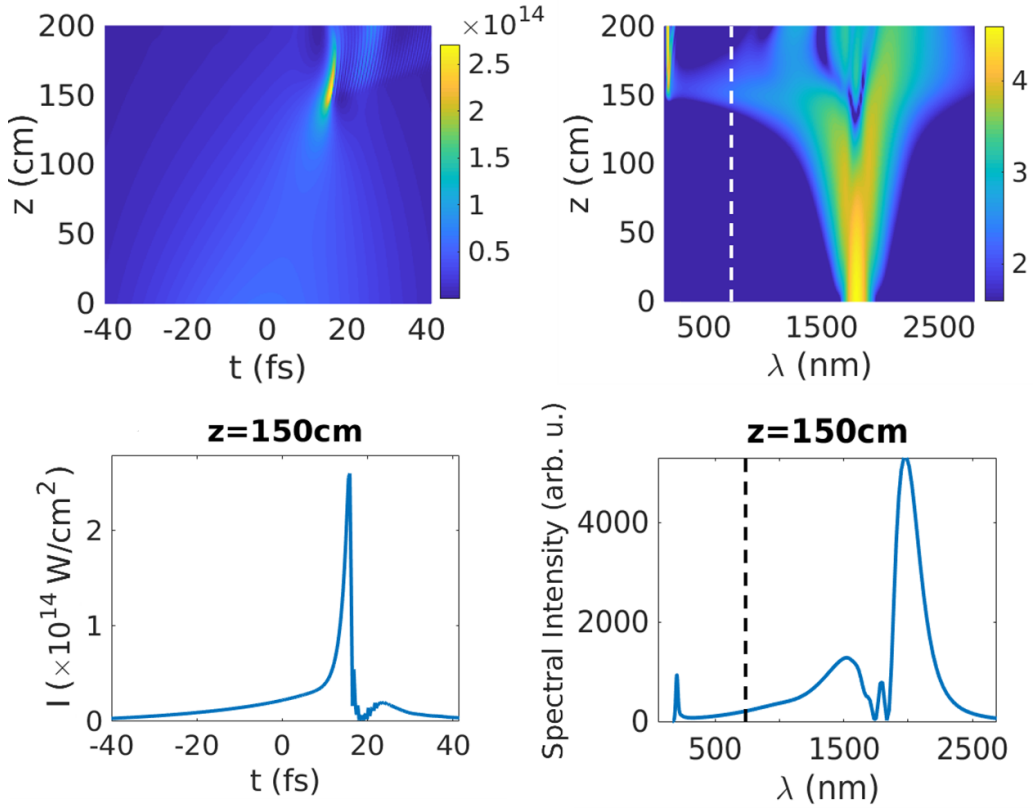

Figure 9. Temporal intensity ($\mathrm{W\,cm^{-2}}$) evolution (top left) and spectral intensity evolution in log scale (top right) of a 50 fs pulse centred in 1800 nm with 0.62 mJ, propagating inside a HCF with 150 μm core radius filled with Ar at 0.2 bar using the time-dependent (1 + 1)D model. Temporal and spectral intensity profile (bottom left and bottom right respectively) at the point of maximum self-compression (150 cm). The ZDW is represented as dashed lines.

consequence, to obtain the resonant energy transfer, the pump and the DW wavelengths must lie in opposite sides of the ZDW. We use the time-dependent (1 + 1)D model to simulate the nonlinear propagation of the fundamental spatial mode of a HCF, the EH_{11} mode. The initial condition used to solve numerically equation (50) is

$$A(r,T,z=0) \propto \begin{cases} J_0\left(u_{11}r/r_F\right) & r \leqslant r_F \\ 0 & r > r_F \end{cases} . \qquad (62)$$

We simulate the propagation of a 50-fs laser pulse with 0.62 mJ input energy and centred at 1800 nm inside a 2-meter long HCF with 150 μm core radius filled with argon at 0.2 bar. We use the expression for the linear refractive index of argon given in [61] and the corresponding nonlinear refractive index is $n_{NL} = 1.74 \times 10^{-23} \cdot p$ ($\mathrm{m^2\,W^{-1}}$), where p is the gas pressure in bar [62]. For these particular parameters, the zero-dispersion wavelength is 737 nm, which means that the dispersion of the pump pulse is anomalous.

In figure 9 we show the (1 + 1)D propagation dynamics. The top-left panel shows the evolution of the temporal intensity distribution, while the top-right panel shows the evolution of the spectral intensity distribution. Both panels represent the characteristic propagation dynamics in a self-compression process. It is clear from figure 9 (top left), that the pulse duration, which is initially 50 fs, becomes shorter along the propagation until it reaches 2.18 fs, below one-cycle duration for a pump wavelength of 1800 nm due to the spectral broadening achieved. This optimal pulse self-compression occurs at $z_{sc} = 150$ cm inside the HCF.

On the other hand, in figure 9 (top right), we can observe a symmetric spectral broadening due to self-phase modulation and, at the point of optimal pulse self-compression, the spectrum expands shedding energy in the ultraviolet region (normal dispersion region). This emission at 204 nm is in good agreement with the DW wavelength predicted from the phase matching condition, equation (59), for these parameters. In figure 9, bottom left and right panels represent the temporal and spectral intensity profile at the point of maximum self-compression (150 cm), respectively. In bottom-left panel, the self-compressed pulse at 150 cm inside the HCF presents an intensity profile with features from a soliton self-compression process. It has a long front tail and the peak of the pulse located at the trailing part. The generated DW propagates at a different group velocity and, at some point, it interferes with the soliton causing the appearance of some amplitude oscillations at the trailing part of the pulse [23]. In the spectral intensity profile at 150 nm (bottom-right), we can observe the spectral broadening and the emission of a DW at 204 nm. Since the DW lies in the normal dispersion region, it broadens as it propagates away

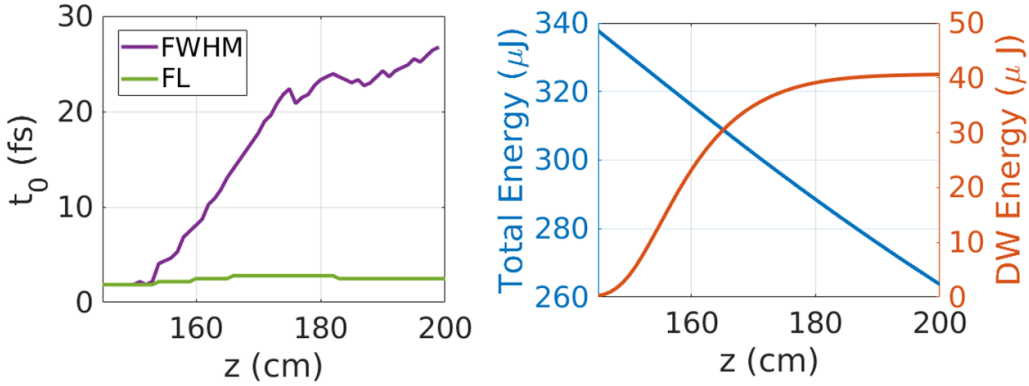

Figure 10. Left panel shows the evolution of the FWHM temporal duration (purple line) and Fourier Limit duration (green line) of the generated DW. Right panel shows the evolution of the total pulse energy (blue line) and the energy of the DW (orange line) from the emission point to the HCF output.

from the soliton, which explains the second structure behind the main peak observed in figure 9 (bottom-left).

To use this emission as an ultrashort source, we have to calculate its duration and the amount of energy transferred to it from the soliton. For this reason, we have filtered the DW spectrally and reconstructed the temporal structure of the ultraviolet pulse for the case presented in figure 9 (1800 nm, 50 fs, 0.62 mJ and Ar at 0.2 bar). In figure 10 (left), we show the evolution of the full width half maximum (FWHM) duration of the DW (purple line) and the corresponding Fourier Limit (green line) from z_{sc}, the point where the DW is generated, to the HCF output. At z_{sc}, the FWHM duration of the DW is 1.87 fs, the same as the Fourier Limit and also similar to the FWHM duration of the soliton at z_{sc}. However, despite the low pressure, as the DW propagates in the normal dispersion region of the HCF it broadens reaching 26.75 fs at the HCF output.

Figure 10 (right) shows the energy of the DW (orange line) together with the total energy of the pulse (blue line). We can see that at the point of the DW emission (z_{sc}) the energy is low, less than 4 μJ, but as it propagates in the HCF more energy is transferred from the soliton until it saturates, reaching 40.62 μJ at the HCF output. The efficiency of the process will be limited by the phase-matching between the DW and the soliton, the self-compression process and the consequent spectral broadening, the temporal overlap between the soliton and the DW and other high-order effects that complicate the propagation of the pulse in the HCF. We can deduce that it is possible to obtain an ultrashort source from the DW, if the emission occurs near the HCF output, but the energy would be low. On the contrary, if we are interested in an energetic DW, the more it propagates inside the HCF the more energy it gains, but its duration grows along the propagation.

4.2. Role of the spatial modes in the DW emission process

Another feature we can study is the multimode nature of the DW generation process and the influence of the spatial dynamics and the ionization of the medium. So far, we have studied the DW generation process with the time-dependent (1 + 1)D model. This model includes neither the spatial dynamics nor the ionization, so the simulations are single mode and the energy transfer between the soliton and the DW always occurs in the same spatial mode. However, taking into account the spatial dynamics could lead to the emission of different DWs that might be related with the appearance of other spatial modes, besides the fundamental mode [26], and the generation of plasma.

We have performed the same propagation with the (2 + 1)D model (1800 nm, 50 fs, 0.62 mJ and Ar at 0.2 bar). The propagation dynamics is similar with both models, meaning that neither the spatial dynamics nor the ionization are significant during the propagation in this case. However, there is a small disagreement near the DW generation point (150 cm). We can see in figure 11 a comparison of the spectral intensity profile of the DW obtained with the time-dependent (1 + 1)D model and the (2 + 1)D model at 150 cm (left) and at the HCF output (centre). There is a red shift of the DW wavelength obtained with the (2 + 1)D model and the differences between both models are more important at the HCF output. The DW obtained from the (2 + 1)D model is significantly more structured than the one obtained with the (1 + 1)D model. Although it is hard to identify the exact origin of this structure it must be related to the ionization and the multimode nature of the propagation, that is only kept by the (2 + 1)D model.

To expose the relevance of the higher spatial modes obtained with the (2 + 1)D model in this particular situation, figure 11 (right) shows the mode decomposition of the DW, illustrating the substantial contribution of different spatial modes to the emission of the DW along the propagation.

4.3. Fixed DW emission for different pump wavelengths

In this subsection we will study the possibility of generating a DW at a fixed wavelength, in a one-step process, using different pump wavelengths. We have chosen 150 nm as a target wavelength for the DW emission, due to its possible interest in nuclear clocks based on ^{229}Th thorium isomer [63, 64]. Following the theoretical predictions, using neon at 0.5 bar with a 35 fs pump pulse centred at 800 nm is suitable for the DW generation at 150 nm, and this will be our reference case.

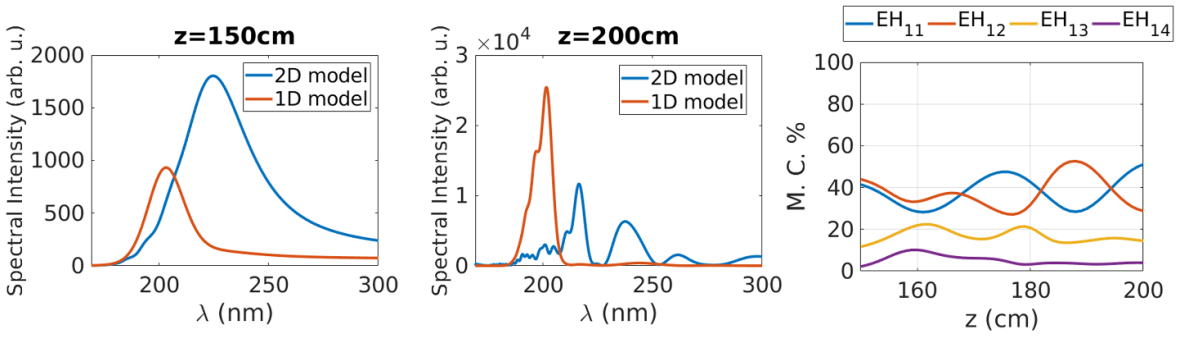

Figure 11. Spectral intensity profile of the DW from the time-dependent $(1+1)$D model (orange line) and the $(2+1)$D model (blue line) at 150 cm (left) and at the HCF output (centre). Right panel shows the mode contribution of the first four spatial modes to the DW.

We perform a simulation using the $(1+1)$D temporal model of the EH_{11} mode with 35 fs and 0.33 mJ inside a HCF with 100 μm of core radius filled with neon at 0.5 bar. The nonlinear refractive index of neon is $n_{NL} = 0.14 \times 10^{-23} \cdot p$ $(\mathrm{m^2\,W^{-1}})$ [62], p being the gas pressure in bar, and for the linear refractive index we use the expression in [65]. With the chosen parameters, the ZDW (419 nm) is shorter than the pump wavelength and we expect to activate the self-compression process, the subsequent soliton formation and the generation of the DW. Performing the simulation, we can obtain the DW at 150 nm after 290 cm of propagation inside the HCF (see figure 12(c)).

To obtain the same dynamics using another pump wavelength, the interaction between nonlinearity and dispersion in the propagation must be similar. Since the dispersion of the HCF depends on the laser and HCF parameters, we have to select them carefully.

We find the scaling rules to obtain the same DW generation process for different pump wavelengths in approximately the same distance inside the HCF. The method we have followed to obtain the same interaction between the dispersion and the nonlinearity, taking as a reference the 800 nm case, consists in several steps:

4.3.1. Pulse duration. The first thing we change to obtain the same dispersion is the pulse duration, t_0, to match the number of cycles, n_c, of the new pump wavelength, $\lambda^{(2)}$, with the 800 nm case, $\lambda^{(1)}$.

$$t_0^{(2)} = n_c^{(1)} \frac{c}{\lambda^{(2)}} = \frac{\lambda^{(2)}}{\lambda^{(1)}} t_0^{(1)} \tag{63}$$

where c is the velocity of light in vacuum. Therefore, the duration of the new pulse, $t_0^{(2)}$, will be fixed and related with the duration of the reference one, $t_0^{(1)}$.

4.3.2. HCF core radius. Assuming that the losses of the pulse during the propagation correspond to the HCF itself and they do not depend on the pressure of the filling gas, the next parameter we have to change to obtain the same dynamics is the HCF size. This way we obtain the same propagation losses with the new pump wavelength $\lambda^{(2)}$.

The HCF losses are given by the absorption coefficient α_{pq} defined in equation (39). From this equation we assume that the losses are related with the pump wavelength and the HCF core radius as

$$\alpha \approx \frac{\lambda^2}{{r_F}^3}. \tag{64}$$

Matching the absorption coefficients of the new pump wavelength with the coefficient of the reference case, we obtain the corresponding relation between the HCF core radii

$$r_F^{(2)} = \left(\frac{\lambda^{(2)}}{\lambda^{(1)}}\right)^{2/3} r_F^{(1)}. \tag{65}$$

Therefore, the core size of the new HCF, $r_F^{(2)}$, must be related to the core size of the HCF used with the reference pump wavelength, $r_F^{(1)}$. Until this point, equations (63) and (65) suggest that the scaling parameter could be $(\lambda^{(2)}/\lambda^{(1)})$.

4.3.3. Gas pressure. By changing the gas pressure we also adjust the dispersion of the new wavelength, $\lambda^{(2)}$, to be the same as the reference case, $\lambda^{(1)}$. A different gas pressure modifies the location of the ZDW, but not the location of the phase-matching wavelength for the DW emission, as we have already scaled the core radius.

Since longer wavelengths induce a blue shift, and higher gas pressures lead to a red shift in the DW emission, we change the gas pressure as follows

$$p^{(2)} = \frac{\lambda^{(2)}}{\lambda^{(1)}} p^{(1)}. \tag{66}$$

4.3.4. Pulse energy. With the scaling of the pulse duration, the core radius and the gas pressure, we have adjusted the dispersion of the pulse to be the same as the reference case. We also have to adjust the nonlinearity that the pulse experiences in the propagation. For this purpose, we scale the input pulse energy comparing the nonlinear phase accumulated during the propagation through the B-integral,

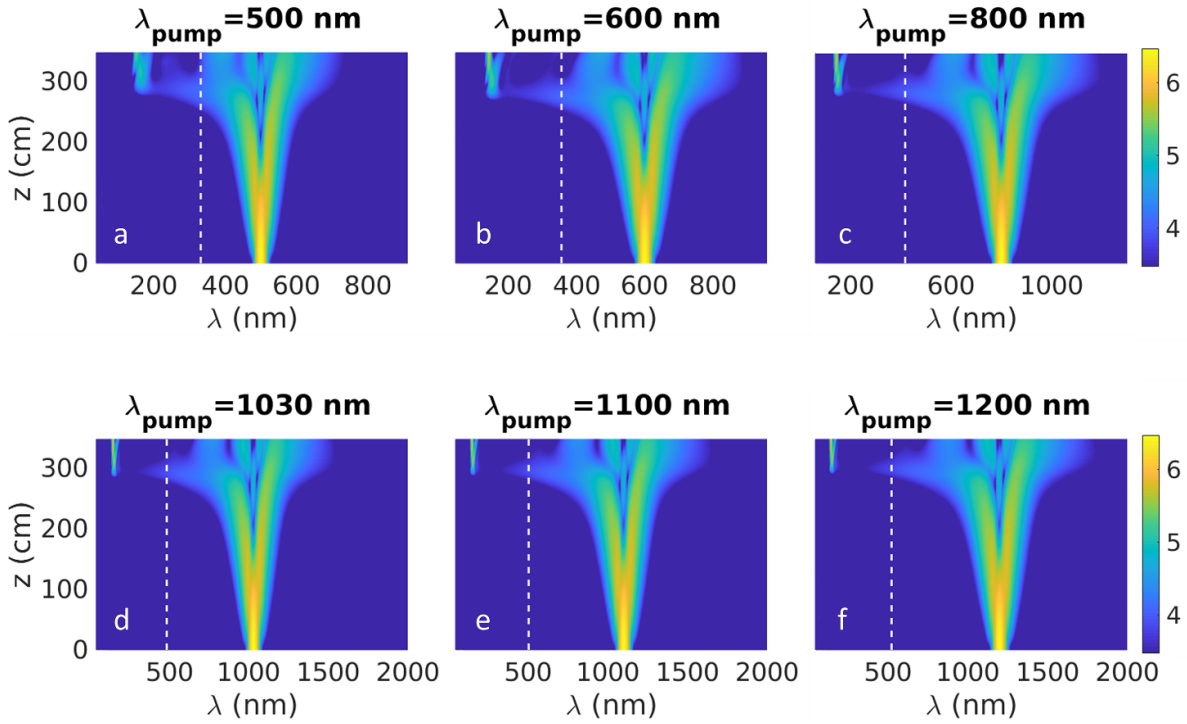

Figure 12. Spectral intensity evolution in log scale along the propagation in the HCF for different pump wavelengths using the time-dependent (1 + 1)D model. The ZDWs are represented as white dashed lines.

Table 1. Laser and HCF parameters for different pump wavelengths, (λ_p), obtained from the scaling rules: the input FWHM duration (t_0), HCF core radius (r_F), Ne pressure (p) and input pulse energy (E_{in}). The last column shows the zero-dispersion wavelength (ZDW) in each case.

λ_p (nm)	t_0 (fs)	r_F (μm)	p (bar)	E_{in} (mJ)	λ_{ZD} (nm)
500	22.04	73.10	0.33	0.10	332
600	26.45	82.55	0.35	0.17	340
800	35.26	100.00	0.47	0.33	419
1030	45.48	118.35	0.61	0.59	484
1100	48.56	123.65	0.65	0.69	503
1200	52.98	131.04	0.69	0.86	525

$B = 2\pi/\lambda \int_0^{L_F} (n_{NL} \cdot p) I_0 dz$, being L_F the length of the fibre and I_0 the input intensity,

$$B^{(1)} = B^{(2)} \rightarrow I_0^{(2)} = \frac{\lambda^{(2)}}{\lambda^{(1)}} \frac{p^{(1)}}{p^{(2)}} I_0^{(1)} \tag{67}$$

where we have assumed that n_{NL} is proportional to the pressure, which is a good approximation at low and moderate pressures. We use the input pulse intensity as an estimation and we assume that it is constant along the propagation, since we do not know how the intensity evolves in advance. We can describe the intensity as a function of the energy of the pulse through the following relation

$$E = \int I(r,\theta,t) dr d\theta dt = \pi {r_F}^2 \left(J_1(u_{01})\right)^2 I_0 I_t. \tag{68}$$

I_t being the integral of the temporal intensity distribution. For simplicity, we assume a Gaussian distribution, so the temporal intensity distribution can be expressed as $I_t = \sqrt{\pi/2} t_0$. The relation between the input energies can be written as

$$E^{(2)} = \left(\frac{\lambda^{(2)}}{\lambda^{(1)}}\right)^{7/3} E^{(1)}. \tag{69}$$

Again, for longer wavelengths the input energy is higher, which is translated into a blue-shift of the DW.

We have developed this scaling route to obtain the same nonlinear dynamics in the HCF and it works within our model. There are other strategies to implement a similar parameter scaling in the literature to obtain the same nonlinear propagation [23, 66–69]. Using the scaling rules defined above, we have performed a wavelength scan from 500 to 1200 nm. In table 1 we show the different laser and HCF parameters obtained for each pump wavelength using the time-dependent (1 + 1)D model.

In figure 12 we can observe a comparison of the nonlinear propagation dynamics obtained with the time-dependent (1 +

1)D model for the different pump wavelengths presented in table 1. We show the evolution of the spectral intensity distribution in logarithmic scale in each case. We observe that the spectral broadening dynamics is almost identical and between 300 and 350 cm inside the HCF the DW is emitted at 150 nm.

Since the input pulse in all the cases experiences anomalous dispersion at the beginning of the propagation (check the ZDW values in table 1), a soliton self-compression effect is always observed. For each pump wavelength, the DW generation process occurs at similar distances inside the HCF (290 cm), as expected. To validate the results, we have checked that neither the ionization nor the spatial dynamics play a significant role in this regime, performing the same simulations but with the (2 + 1)D model and obtaining very similar results.

5. Summary

In this work, we present the theoretical model and the different numerical strategies to study the nonlinear propagation of a laser pulse inside a HCF in different scenarios. We explain diverse numerical models, time-independent (1 + 1)D model, spatio-temporal (2 + 1)D model and non-cylindrical symmetry (3 + 1)D model, depending on the effects and dynamics under study.

As a particular case, we have studied the DW emission process and different features in the dynamics, such as the temporal duration, energy and the role of the high-order modes in the propagation. We have checked the parameter scaling route we have proposed to obtain a DW at a certain wavelength for different pump wavelengths.

Data availability statement

All data that support the findings of this study are included within the article (and any supplementary files).

Acknowledgment

This work has been financed by Ministerio de Economía y Competitividad (BES-2017-080280) and Ministerio de Ciencia e Innovación (PID2019-106910GB-I00). A C acknowledges funding from the Ministerio de Universidades and the European Union NextGenerationEU/PRTR via her Margarita Salas Fellowship through the University of Salamanca.

ORCID iDs

Aurora Crego https://orcid.org/0000-0002-1632-5745
Julio San Roman https://orcid.org/0000-0002-2645-7039
Enrique Conejero Jarque https://orcid.org/0000-0002-5328-6714

References

[1] Kao K C and Hockham G A 1966 *IEE Proc.* **133** 191–8
[2] Shank C V, Fork R L, Yen R, Stolen R H and Tomlinson W J 1982 *Appl. Phys. Lett.* **40** 761–3
[3] Fork R L, Brito Cruz C H, Becker P C and Shank C V 1987 *Opt. Lett.* **12** 483–5
[4] Strickland D and Mourou G 1985 *Opt. Commun.* **56** 219–21
[5] Knight J C, Birks T A, Russell P St J and Atkin D M 1996 *Opt. Lett.* **21** 1547–9
[6] Benabid F, Knight J C, Antonopoulos G and Russell P St J 2002 *Science* **298** 399–402
[7] Nisoli M, De Silvestri S and Svelto O 1996 *Appl. Phys. Lett.* **68** 2793–5
[8] Conejero Jarque E, San Roman J, Silva F, Romero R, Holgado W, Gonzalez-Galicia M A, Sola I J and Crespo H 2018 *Sci. Rep.* **8** 2256
[9] Corkum P B 1993 *Phys. Rev. Lett.* **71** 1994–7
[10] Schweinberger W, Sommer A, Bothschafter E, Li J, Krausz F, Kienberger R and Schultze M 2012 *Opt. Lett.* **37** 3573–5
[11] Anderson A *et al* 2011 *Appl. Phys.* B **103** 531–6
[12] Nisoli M, Sansone G, Stagira S, Vozzi C, De Silvestri S and Svelto O 2002 *Appl. Phys.* B **75** 601–4
[13] Schenkel B, Biegert J, Keller U, Vozzi C, Nisoli M, Sansone G, Stagira S, De Silvestri S and Svelto O 2003 *Opt. Lett.* **28** 1987–9
[14] Suda A, Hatayamab M, Nagasaka K and Midorikawa K 2005 *Appl. Phys. Lett.* **86** 111116
[15] Nagy T, Forster M and Simon P 2008 *Appl. Opt.* **47** 3264–8
[16] Nagy T, Kretschmar M, Vrakking M J J and Rouzée A 2020 *Opt. Lett.* **45** 3313–6
[17] Beetar J E *et al* 2020 *Sci. Adv.* **6** eabb5375
[18] Bohman S, Suda A, Kanai T, Yamaguchi S and Midorikawa K 2010 *Opt. Lett.* **35** 1887–9
[19] Voronin A A and Zheltikov A M 2008 *Phys. Rev.* A **78** 063834
[20] Kretschmar M, Brée C, Nagy T, Demircan A, Kurz H G, Morgner U and Kovačev M 2014 *Opt. Express* **22** 22905–16
[21] Shumakova V, Malevich P, Ališauskas S, Voronin A, Zheltikov A M, Faccio D, Kartashov D, Baltuška A and Pugžlys A 2016 *Nat. Commun.* **7** 12877
[22] Ermolov A, Heide C, Dienstbier P, Köttig F, Tani F, Hommelhoff P and Russell P St J 2019 *Opt. Lett.* **44** 5005–8
[23] Travers J C, Grigorova T F, Brahms C and Belli F 2019 *Nat. Photon.* **13** 547–54
[24] Fernández Galán M, Conejero Jarque E and San Roman J 2022 *Opt. Express* **30** 6755–67
[25] López-Zubieta B A, Conejero Jarque E, Sola I J and San Roman J 2018 *Opt. Express* **26** 6345–50
[26] López-Zubieta B A, Conejero Jarque E, Sola I J and San Roman J 2018 *OSA Contin.* **1** 930–8
[27] Wan Y and Chang W 2021 *Opt. Express* **29** 7070–83
[28] Brahms C and Travers J C 2022 *J. Phys. Photon.* **4** 034002
[29] Crego A, Conejero Jarque E and San Roman J 2021 *Opt. Express* **29** 929–37
[30] Novoa D, Cassataro M, Travers J C and Russell P St J 2015 *Phys. Rev. Lett.* **115** 033901
[31] Cassataro M, Novoa D, Günendi M C, Edavalath N N, Frosz M H, Travers J C and Russell P St J 2017 *Opt. Express* **25** 7637–44
[32] Ugaitz E *et al* 2021 *Nat. Photon.* **15** 277–80
[33] Brahms C, Grigorova T, Belli F and Travers J C 2019 *Opt. Lett.* **44** 2990–3
[34] Borrego Varillas R, Candeo A, Viola D, Garavelli M, De Silvestri S, Cerullo G and Manzoni C 2014 *Opt. Lett.* **39** 3849–52
[35] Chang K F, Reduzzi M, Wang H, Poullain S M, Kobayashi Y, Barreau L, Prendergast D, Neumark D M and Leone S R 2020 *Nat. Commun.* **11** 4042
[36] Durfee C G, Backus S, Murnane M M and Kapteyn H C 1997 *Opt. Lett.* **22** 1565–7

[37] Jiang X, Joly N, Finger M, Babic F, Wong G, Travers J and Russell P St J 2015 *Nat. Photon.* **9** 133–9
[38] Beutler M, Ghotbi M, Noack F and Hertel I V 2010 *Opt. Lett.* **35** 1491–3
[39] Galli M *et al* 2019 *Opt. Lett.* **44** 1308–11
[40] Zhang C *et al* 2022 *Opt. Lett.* **47** 4830–3
[41] Boyd R 2020 *Nonlinear Optics* 4th edn (New York: Academic)
[42] Couairon A and Mysyrowicz A 2007 *Phys. Rep.* **441** 47–189
[43] Agrawal G P 2013 *Nonlinear Fiber Optics* 5th edn (New York: Academic)
[44] Brabec T and Krausz F 1997 *Phys. Rev. Lett.* **78** 3282–5
[45] Marburger J H 1975 *Prog. Quantum Electron.* **4** 35–110
[46] Brabec T and Krausz F 2000 *Rev. Mod. Phys.* **72** 545–91
[47] Couairon A, Tzortzakis S, Bergé L, Franco M, Prade B and Mysyrowicz A 2002 *J. Opt. Soc. Am.* B **19** 1117–31
[48] Bloembergen N 1973 *Opt. Commun.* **8** 285–8
[49] Couairon A, Brambilla E, Corti T, Majus D, Ramírez-Góngora O de J and Kolesik M 2011 *Eur. Phys. J. Spec. Top.* **199** 5–76
[50] Perelomov A M, Popov V S and Terent'ev M V 1966 *JTPHES* **23** 924–34 (available at: http://jetp.ras.ru/cgi-bin/dn/e_023_05_0924.pdf)
[51] Marcatili E A J and Schmeltzer R A 1964 *Bell Syst. Tech. J.* **43** 1783–809
[52] Homoelle D and Gaeta A L 2000 *Opt. Lett.* **25** 761–3
[53] Kudryashov N A 1988 *J. Appl. Math. Mech.* **52** 361–5
[54] Wang M, Li X and Zhang J 2008 *Phys. Lett.* A **372** 417–23
[55] He J H and Wu X H 2006 *Chaos Solitons Fractals* **30** 700–8
[56] Dan J, Sain S, Ghose-Choudhury A and Garai S 2020 *Optik* **224** 165519
[57] Kelley P L 1965 *Phys. Rev. Lett.* **15** 1005–8
[58] He F, Ruiz C and Becker A 2007 *Phys. Rev.* A **75** 053407
[59] Guizar-Sicairos M and Gutiérrez-Vega J C 2004 *J. Opt. Soc. Am.* A **21** 53–58
[60] Rothenberg J E 1992 *Opt. Lett.* **17** 1340–2
[61] Zhang J, Lu Z H and Wang L J 2008 *Appl. Opt.* **47** 3143–51
[62] Couairon A, Chakraborty H S and Gaarde M B 2008 *Phys. Rev.* A **77** 053814
[63] Peik E and Tamm C 2003 *Europhys. Lett.* **61** 181–6
[64] Campbell C J, Radnaev A G, Kuzmich A, Dzuba V A, Flambaum V V and Derevianko A 2012 *Phys. Rev. Lett.* **108** 120802
[65] Dalgarno A and Kingston A E 1960 *Proc. R. Soc.* A **259** 424–31
[66] Chen C M and Kelley P L 2002 *J. Opt. Soc. Am.* B **19** 1961–7
[67] Böhle F *et al* 2014 *Laser Phys. Lett.* **11** 095401
[68] Heyl C M *et al* 2016 *Optica* **3** 75–81
[69] Fan G, Carpeggiani P A, Tao Z, Coccia G, Safaei R, Kaksis E, Pugzlys A, Légaré F, Schmidt B E and Baltuška A 2021 *Opt. Lett.* **46** 896–9